ORIGINAL PAPER

Nano- and micro-structures in lunar zircon from Apollo 15 and 16 impactites: implications for age interpretations

Monika A. Kusiak[1] · Elizaveta Kovaleva[2,3] · Dennis Vanderliek[4] · Harry Becker[4] · Franziska Wilke[3] · Anja Schreiber[3] · Richard Wirth[3]

Abstract

Meteorite impact processes are ubiquitous on the surfaces of rocky and icy bodies in the Solar System, including the Moon. One of the most common accessory minerals, zircon, when shocked, produces specific micro-structures that may become indicative of the age and shock conditions of these impact processes. To better understand the shock mechanisms in zircon from Apollo 15 and 16 impact breccias, we applied transmission electron microscopy (TEM) and studied nano-structures in eight lunar zircons displaying four different morphologies from breccias 15455, 67915, and 67955. Our observations revealed a range of shock-related features in zircon: (1) planar and non-planar fractures, (2) "columnar" zircon rims around baddeleyite cores, (3) granular textured zircon, in most cases with sub-μm-size inclusions of monoclinic ZrO_2 (baddeleyite) and cubic ZrO_2 (zirconia), (4) silica-rich glass and metal inclusions of FeS and FeNi present at triple junctions in granular zircon and in baddeleyite, (5) inclusions of rutile in shocked baddeleyite, (6) amorphous domains, (7) recrystallized domains. In many grain aggregates, shock-related micro-structures overprint each other, indicating either different stages of a single impact process or multiple impact events. During shock, some zircons were transformed to diaplectic glass (6), and others (7) were completely decomposed into SiO_2 and Zr-oxide, evident from the observed round shapes of cubic zirconia and silica-rich glass filling triple junctions of zircon granules. Despite the highly variable effect on textures and Zr phases, shock-related features show no correlation with relatively homogeneous U–Pb or $^{207}Pb/^{206}Pb$ ages of zircons. Either the shock events occurred very soon after the solidification or recrystallization of the different Zr phases, or the shock events were too brief to result in noticeable Pb loss during shock metamorphism.

Keywords Lunar zircon · Nanostructures · Zircon textures · Baddeleyite · Cubic zirconia

Communicated by Othmar Müntener.

✉ Monika A. Kusiak
monika.kusiak@igf.edu.pl

1   Institute of Geophysics, Polish Academy of Sciences, 01452 Warsaw, Poland

2   University of the Western Cape, Robert Sobukwe Road, Bellville 7535, South Africa

3   Helmholtz Centre Potsdam, GFZ German Research Centre for Geosciences, 3.5 Interface Geochemistry, 14473 Potsdam, Germany

4   Institute for Geological Sciences, Freie University, 12249 Berlin, Germany

Introduction

Zircon [ZrSiO₄], is one of the most common accessory mineral, and due to its robustness against isotopic resetting, it is widely used as U–Pb geochronometer for terrestrial and lunar samples (Nemchin et al. 2012). The preferred incorporation of U into the zircon lattice and two U–Pb decay systems with different decay constants, permit using two independent geochronometers in the same mineral, increasing the effectiveness of dating (Davis et al. 2003). Furthermore, zircon can maintain geochemical information through various overprinting events and record complex histories. Individual zircon grains can preserve not only information of primary igneous crystallization processes (e.g., Corfu et al. 2003 and references therein), but also partial/complete recrystallization or replacement (e.g., Kusiak et al. 2014), records of metamorphic heating (e.g., Dunkley et al. 2020;

Rubatto 2017) or ductile deformation events related to geodynamic processes (e.g., Piazolo et al. 2012).

During impact events on planetary bodies, the U–Pb system in zircon recovered from impactites can be partially or completely reset, and different structural domains in zircon can provide not only primary igneous crystallization ages but also ages of subsequent impact events. This effect was documented by studies of both terrestrial and lunar zircons (e.g., Cavosie et al. 2016; Crow et al. 2017; Grange et al. 2009; Kenny et al. 2019; Nemchin et al. 2009; Thiessen et al. 2018). Therefore, for the appropriate age interpretation of shocked zircons in terms of associated impact events, it is crucial to investigate and understand the origin of micro- and nano-structures in individual grains of this mineral. Several previous studies (Crow et al. 2017; 2019; Grange et al. 2013b; Leroux et al. 1999; Moser et al. 2009; 2011; Timms et al. 2012; Wittmann et al. 2006; Wielicki and Harrison 2015) documented the variability of micro- and nano-structures in shocked terrestrial and lunar zircons. For example, polycrystalline (granular neoblastic) shocked zircon grains from the Vredefort impact structure provide isotopic ages that are consistent with the age of the Vredefort impact event (Cavosie et al. 2015). These zircons also record nanoscale evidence of complete shock decomposition to ZrO_2 and SiO_2 and melting with subsequent crystallization of zircon from molten domains (Kovaleva et al. 2021). Evidence for local shock melting of zircon also provides constraints on the temperature of the process, which should have exceeded the melting temperature of zirconium oxide (ca. 2715 °C).

Even though many U–Pb and Pb/Pb geochronological studies were dedicated to zircons from lunar impactites (Bellucci et al. 2016; 2019; Crow et al. 2017; Grange et al. 2009; 2013b; Nemchin et al. 2012; Pidgeon et al. 2007; Trail et al. 2020; Vanderliek et al. 2021a), only a few of them investigated the details of zircon deformation micro-structures (e.g., Crow et al. 2019; Nemchin et al. 2012; Timms et al. 2012). Grange et al. (2013b) emphasized the importance of recognition and understanding of secondary features in shocked lunar zircon grains especially for in situ age dating of deformed or recrystallized areas of the crystal lattice.

Here we present results of the study of eight lunar zircon grains from samples 15455 (Apollo 15), 67915 and 67955 (Apollo 16), combining focused ion beam (FIB) extraction of thin foils with transmission electron microscopy (TEM) investigations, supplemented by scanning electron microscopy (SEM) and electron microprobe (EMP) analysis. The purpose of this study is to describe a range of shock-related nano-structures to extend the limited database of lunar zircon textures and to facilitate the interpretation of the U–Pb data obtained on these zircons (e.g., Vanderliek et al. 2021a). Since some U–Pb age data on zircons of samples 15455 and 67915 are reversely discordant (Vanderliek et al., 2021a), we evaluated whether the discordance may have been caused

by the Pb mobilization in zircon (Kusiak et al. 2013, 2015; Piazolo et al. 2016) or reflects an analytical artifact (e.g., White and Ireland 2012; Williams and Hergt 2000).

Samples and previous results

For the present study, samples that were petrographically and geochronologically characterized by Vanderliek et al. (2021a and references therein) were selected.

Apollo 15 landing site; dimict breccia 15455

Sample 15455 was collected from the rim of Spur crater and represents a shocked cataclastic anorthositic norite intruded by zircon-free, KREEP-rich impact melt of presumed Imbrian age. Zircon most commonly occurs in silica–diopside bearing domains in the norite and enclosed in plagioclase in local association with baddeleyite and phosphates. Zircon occurs as granular aggregates (mostly < 30 μm), composed of 1–2 μm-sized euhedral zircon neoblasts (Fig. 1C). Previous studies interpreted aggregates of granular zircon in lunar samples as a result of impact-induced recrystallization, presumably in bedrock adjacent to large impact melt sheets (Crow et al. 2017; Vanderliek et al. 2021a and references therein). A few Zr-bearing aggregates (> 30 μm) in this sample represent zircon–baddeleyite intergrowths, with baddeleyite in the center of the aggregate and zircon forming the rim (Fig. 1A, B). Based on seven zircon aggregates analyzed by secondary ion mass spectrometry (SIMS) in Sections 15455,27 and ,29 (11 analyses), the spread of $^{207}Pb/^{206}Pb$ ages is ranging from 4210 to 4154 Ma, with most of the U–Pb data on zircon being concordant and a few analyses reverse discordant (Vanderliek et al. 2021a). Concordant analyses in zircon yield a mean concordia age of 4201 ± 11 Ma, whereas all analyses combined yield a weighted average of 4191 ± 4 Ma. A previous study by Crow et al. (2017) separated large granular zircon aggregates from 15455, which yielded $^{207}Pb/^{206}Pb$ ages near 4.33 Ga. The $^{207}Pb/^{206}Pb$ ages of large baddeleyite intergrown with zircon overlap with the age range near 4.2 Ga obtained on zircons by Vanderliek et al. (2021a); however, some baddeleyites could be slightly older, up to 4.27 Ga (Vanderliek et al. 2021b). In contrast, $^{207}Pb/^{206}Pb$ ages of phosphates in 15455 tend to scatter near 3.92 Ga, the likely age of the Imbrium impact (Nemchin et al. 2021; Vanderliek et al. 2021b).

Apollo 16 landing site; polymict breccia 67915

This breccia was collected during Apollo 16 mission at Station 11 from the rim of the North Ray crater from Outhouse rock (Meyer 2005). The fractured polymict impact breccia consists of fine-grained matrix with different types of lithic
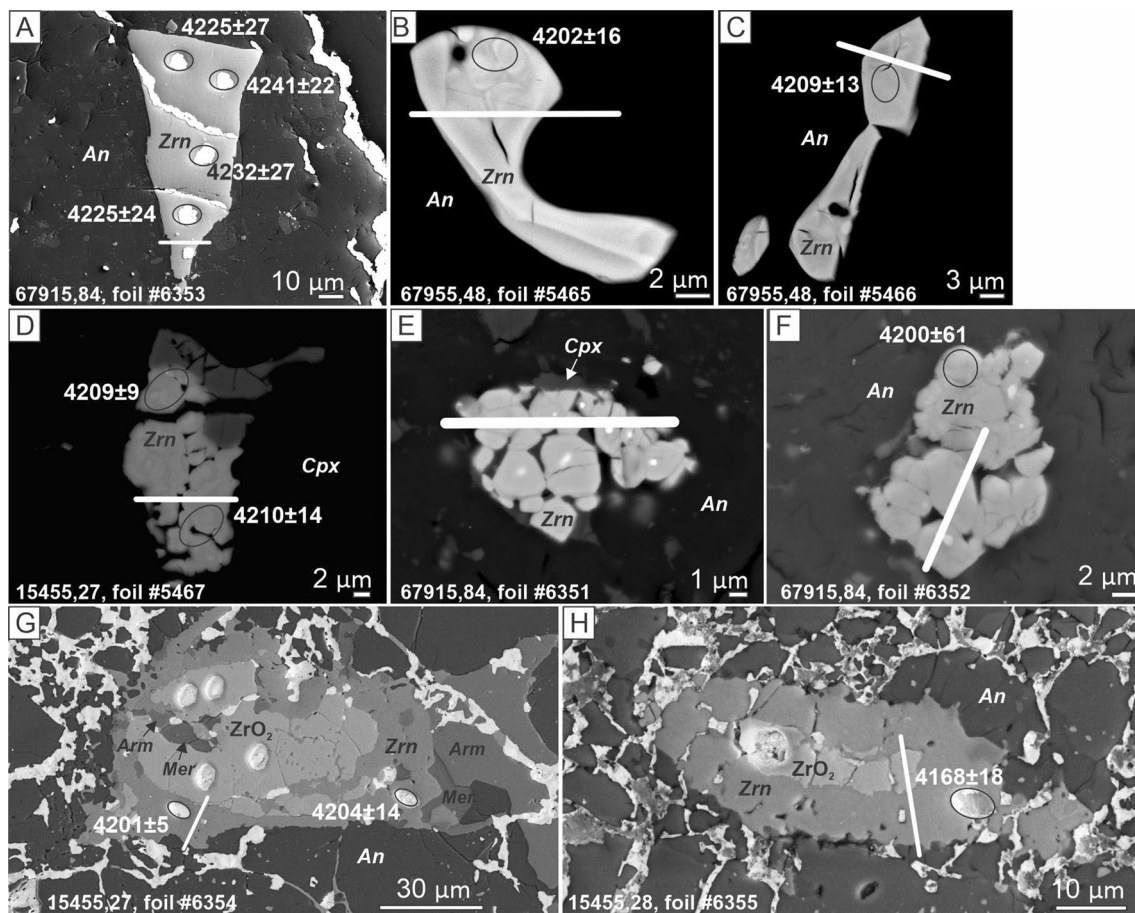
Fig. 1 BSE images of investigated grains and aggregates with white lines indicating the location of the extracted FIB foils. The bright elliptical crater-like structures on the zircon grains are the remains of earlier gold coating in SIMS pits after earlier analyses. Elypses show the exact SIMS spot, the ^{207}Pb/^{206}Pb age is given near each analytical spot. All grains are hosted by anorthite, *An* anorthite, *Ar* armalcolite, *Mer* merrillite, *Zrn* zircon; **A** idiomorphic zircon of triangular shape from sample 67915–84, foil #6353; **B**, **C** subhedral zircons of sample 67955,48, foil #5465 and #5466, respectively. **D** Granular zircon aggregate of sample 15455,27, foil #5467; **E**, **F** granular zircon aggregates of sample 67915,84, foil #6351 and foil #6352, respectively; large bright particle in the middle top is baddeleyite. **G** Baddeleyite surrounded by zircon in anorthite matrix from sample 15455,27, foil #6354; **H** baddeleyite core with zircon rim hosted by anorthite matrix 15455,28, foil #6355;

and mineral clasts, cross-cut by veins of glass. Zircon grains are < 40 μm with subhedral (Fig. 1F) to anhedral shapes, some are poikilitic and rarely granular (Fig. 1D, E; Vanderliek et al. 2021a). In situ ^{207}Pb/^{206}Pb ages of ten zircons (including granular and other types) obtained by SIMS range from 4241 to 4200 Ma, with some reverse discordant analyses (Vanderliek et al. 2021a). A weighted average of 4225 ± 5 Ma was calculated.

Apollo 16 landing site; breccia 67955

This sample was also collected from Outhouse rock at Station 11 (Meyer 2005). It is a cataclastic breccia consisting of noritic anorthosite clasts of variable composition and a finer brecciated matrix of similar composition that

locally contains thin glass veins. Zircon grains are small (< 10–20 μm) and irregularly shaped (Fig. 1G, H; Vanderliek et al. 2021a). Seven zircon grains from this sample were analyzed by SIMS, and all analyses are concordant yielding ^{207}Pb/^{206}Pb ages from 4218 to 4202 Ma (Vanderliek et al. 2021a), consistent with in situ ^{207}Pb–^{206}Pb data on zirconolite and phosphates and Sm–Nd isochron data obtained previously (Norman and Nemchin 2014; Norman et al. 2016).

Altogether eight FIB foils from four thin sections (TS) investigated earlier by SEM and EMP were prepared. Foil #6353 (Fig. 1A) from anhedral zircon of triangular morphology, foils #5465 and #5466 (Figs. 1B, C, respectively) were cut from thin Section 67955,48 and sampled small irregular to subhedral zircon grains. Three foils were granular zircon aggregate: foil #5467 cut from TS 15455,27 (Fig. 1D),

#6351 and #6352 (Fig. 1E, F), both extracted from TS 67915,84. Two foils sampled zircon–baddeleyite aggregates that have a very similar microstructural appearance and internal structure in SEM: foil #6354 from TS 15455,27 (Fig. 1G) and foil #6355 from TS 15455,28 (Fig. 1H).

Methods

Overview images of the zircon aggregates (Fig. 1D–H) were acquired with a Helios G4 UC Dual Beam system (FEI-Thermo Fisher). For that purpose, the Everhart Thornly (ET) and through-the-lens (TL) detectors were used in secondary electron imaging mode (SE) and backscattered electron mode (BSE). The acceleration voltage was set to 5 and 10 keV, respectively. Images in Fig. 1A–C have been acquired using a ZEISS Ultra Plus scanning electron microscope (SEM) using an acceleration voltage of 20 keV (Vanderliek et al., 2021a).

Electron microprobe (EMP) element mapping using the X-ray intensities of Si, Zr, Al, Ti, K, Ca, Fe, Mg, and Y has been applied before preparation of focused ion beam (FIB) foils. Element distribution maps of zircon grains were performed on a JXA8530F+ electron microprobe with a five-wavelength dispersive spectrometer (WDS) so that five elements can be simultaneously semi-quantitatively mapped. 20 kV accelerating voltage and 20 nA beam current were used, and stage or beam scan mode was applied depending on the size of the grains of interest. The dwell time for each pixel was 400 ms. Mapping results were reported in counts per second. The Y concentration displayed in the EMP elemental maps is always below the detection limit of EDX (< 0.2 at. %) and is only detectable in Zr-oxide phase (Supplemental File).

Foils were prepared from zircon for transmission electron microscopy (TEM) study applying the site-specific FIB technique. The TEM foils are 15–20 μm wide, 10–15 μm deep, and 100 nm thick. Details of the technique are given by Wirth (2009).

Analytical and energy-filtered high-resolution transmission electron microscopy (ATEM, HRTEM) using a FEI Tecnai™ G2 F20 X-Twin at GFZ Potsdam operated at 200 kV with a field emission gun (FEG) electron source was utilized for the present study. The TEM is equipped with a post-column Gatan imaging filter (GIF Tridiem). The HRTEM images presented are energy filtered using a 10 eV window on the zero-loss peak. ATEM was performed with an EDAX X-ray analyser equipped with an ultra-thin window. The X-ray intensities were measured in scanning transmission mode (STEM), where the electron beam is serially scanned over a pre-selected area, minimizing mass loss during data acquisition. Structural data such as d_{hkl} spacing and the angles between adjacent lattice planes of minerals

were determined from electron diffraction patterns or diffraction patterns calculated by fast Fourier transform (FFT). The chemical composition of nanoparticles has been determined by EDS analyses focusing an electron beam (very small spot size 8) onto the nanocrystal with an acquisition time of 30 s. The exact location of the electron beam on the nanocrystal was controlled acquiring continuously images (acquisition time 0.2 s) and calculating the diffraction patterns (FFT) from the images.

Results

Microstructures of eight zircon grains enclosed in silicates in breccias 15455, 67915, and 67955 (Table 1) were studied. Five of these grains were selected for phase and chemical composition analysis by EPM elemental mapping (Supplementary File). The TEM foils provide additional information on the third spatial dimension of the zircon grains displayed in the SEM images (Fig. 1).

Anhedral zircon

Foil #6353, thin Section 67915,84

Anhedral fractured zircon of triangular morphology is enclosed in a crystalline anorthite matrix (Fig. 1A). The grain cross section is approximately 100 μm long with a base of approximately 40 μm wide. At the tip of the triangle, small separate fragments of zircon appear to have broken off the main grain (Fig. 2A). The interface of the triangular-shaped zircon with matrix is irregular. Zircon contains minor fractions of Y (Supplementary file). In the TEM foil, zircon appears as a single crystal with fractures, roughly straight crystal faces, and lacks inclusions (Fig. 2). The anorthite matrix is fractured and contains small grains of olivine and clinopyroxene (Fig. 2A). The zircon–anorthite interface is straight with displacements that are linked to the presence of linear structures with a brighter diffraction contrast within the zircon. The brighter linear features are parallel to each other and are interpreted to represent planar fractures (PFs) (Fig. 2B).

Subhedral zircon

Foils #5465 and #5466, thin Section 67955,48

Both grains of subhedral zircon are texturally similar. They have variable thickness varying from 3 to 8 μm (Fig. 1B, C); however, zircon #5466 appears like a distorted melt droplet. Due to the presence of crystalline and non-crystalline (amorphous) domains, the grain is patchy in BSE (backscattered electron, Fig. 3A) and BF (bright field, Fig. 3B) images,

Table 1 FIB foils and type of zircon investigated in this study together with observed features of zircon grains analyzed

Mission	Thin section	$^{207}Pb/^{206}Pb$ Ages [Ma $\pm 2\sigma$]	FIB foil	Zircon type sampled	Zircon features observed
Apollo 15 Dimict breccia comprising pristine anorthositic norite of the Mg suite infiltrated by KREEP-rich impact melt	15455,27	4201 ± 15 4204 ± 14	#6354	Zircon rim surrounding bad-deleyite core	MAN, columnar internal structures (zircon rim is radiating from baddeleyite)
	15455,28	4168 ± 18	#6355		MAN, inclusions of cubic ZrO_2, TiO_2, FeNi and pores in FeS
	15455,27	4209 ± 12 4210 ± 14	#5467	Granular zircon aggregate	MAN
Apollo 16 Complex polymict breccia	67915,84	Not dated	#6351	Granular zircon aggregate	MAN, open radial fractures, ZrO_2 inclusions
	67915,84	4200 ± 61	#6352		MAN, fractures in crystalline domain, ZrO_2 inclusions
	67915,84	4225 ± 24 4232 ± 27 4241 ± 22 4225 ± 27	#6353	Zircon clast with triangular cross section	Planar fractures, metamict lattice
Apollo 16 Noritic anorthosite breccia, cumulates crystallized from an impact melt sheet	67955,48	4202 ± 16	#5465	Irregular, conchoidal zircon	MAN, open fractures
	67955,48	4209 ± 13	#5466	Subhedral zircon	MAN, inclusion trail

Samples, thin sections, number of zircon grain according to Vanderliek et al. (2021a, b)

*Ages from Vanderliek et al. (2021a, b). Note: SIMS ages obtained in the same grain aggregate, but not at the site of the FIB foil

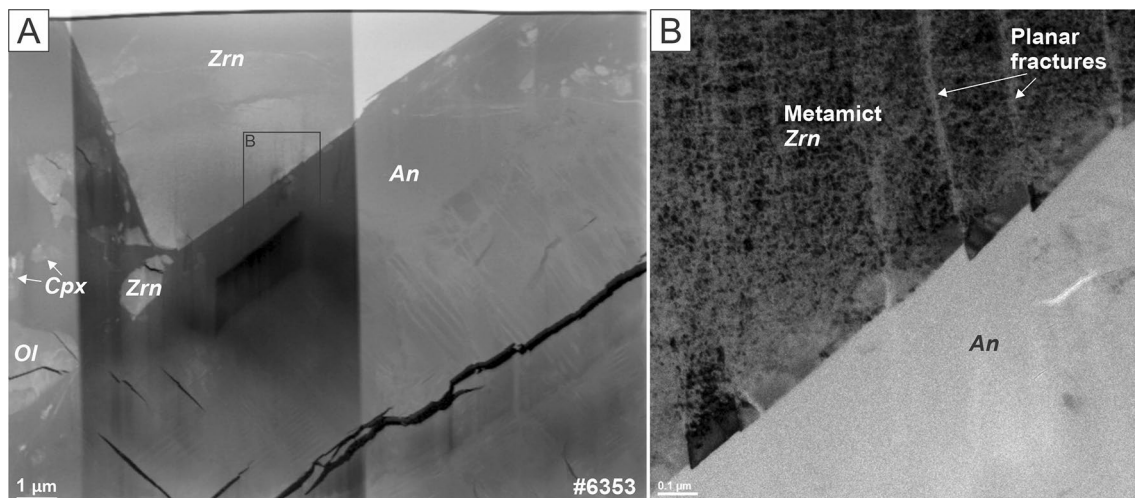*MAN* Mosaic crystal, Amorphous domains, Nanocrystals of recrystallised zircon

Fig. 2 **A** HAADF image of zircon with a fragmented smaller zircon crystal; **B** the BF image of zircon interface with anorthite; foil #6353. Note the steps at zircon surface (planar fractures)

with darker BSE/brighter BF areas being less crystalline (Figs. 3, 4). In crystalline parts of zircon, distinct open fractures are present. Parts of the grain, which are amorphous, show Y contents above detection limit. Within the crystalline rim, an up to 50 μm long inclusion trail is observed (Fig. 4D). Inclusions have well-defined square shapes with inverse facets and appear to be empty.

Granular zircon

Foil #5467, thin Section 15455,27; and foils #6351 and #6352, thin Section 67915,84

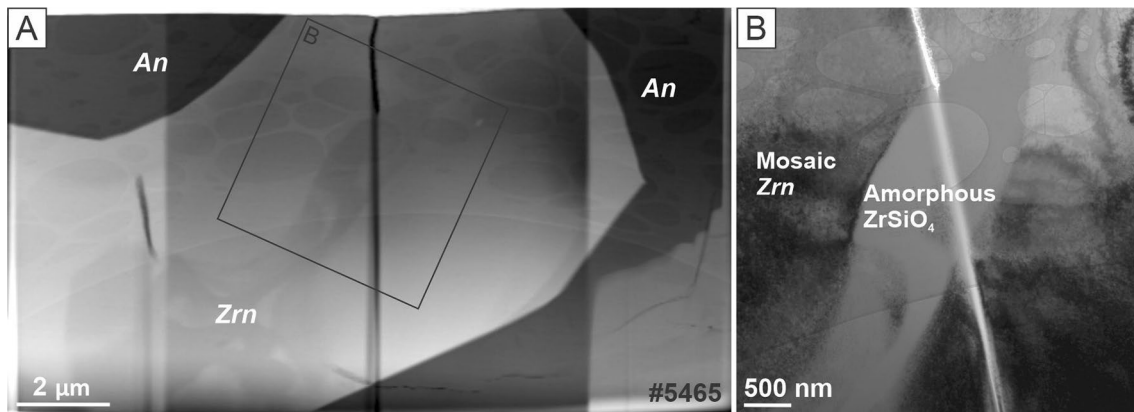Three aggregates of granular zircon were analyzed: #5467 of 28 × 13 μm dimensions (Fig. 1D) hosted by

Fig. 3 **A** HAADF image of an overview of the subhedral zircon; **B** the BF image of area around the crack/open fracture; foil #5465
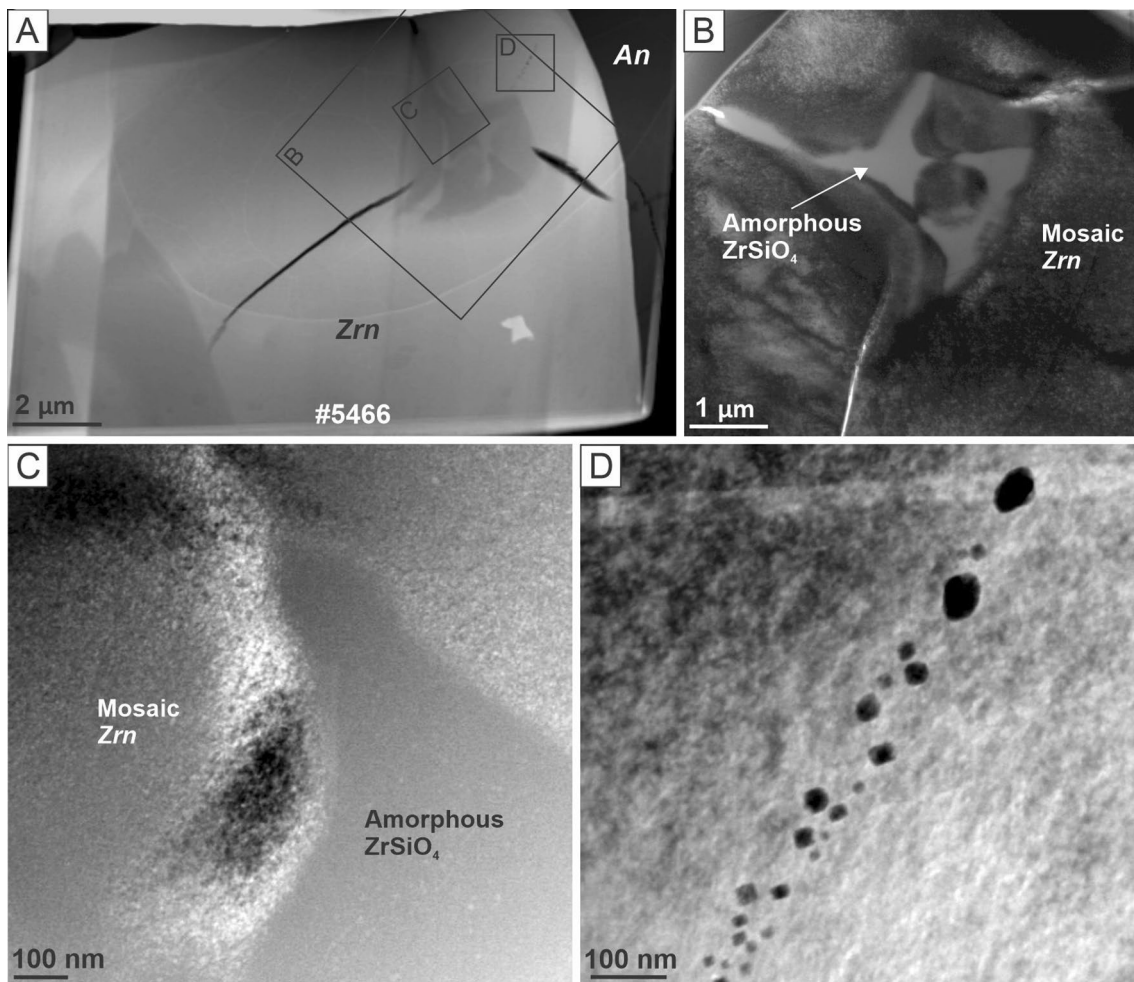

Fig. 4 **A** HAADF image of an overview of the subhedral zircon; foil #5466. **B** HAADF image showing zircon mosaic crystals with amorphous $ZrSiO_4$ in between. Note the round zircon mosaic crystal with contact to two neighboring mosaic crystals forming two sintering necks. **C** BF image. Detail of the interface between two zircon mosaic crystals and amorphous $ZrSiO_4$. **D** HAADF image of a fluid inclusion trail in a mosaic crystal of zircon

clinopyroxene (Cpx; diopside), #6351 of 15×10 μm (Fig. 1E) and #6355 20×12 μm (Fig. 1F), both hosted by anorthite. Granular zircon aggregates reveal individual zircon granules, which represent round or euhedral crystals with variable orientations. Different brightness of zircon in the high-angle annular dark-field (HAADF) Z- and diffraction contrast images (Fig. 6A) reflects the different density within individual granules, which are partially amorphous between crystalline "islands." Cores of the zircon granules are amorphous (lighter grey) whereas their rims are partly crystalline or forming a mosaic crystal (darker grey, Fig. 5C) and often display crystal faces (Figs. 5, 6, 7). Amorphous material is characterized by the absence of

diffraction contrast, for example, along the grain boundaries (diffraction pattern (iii) on Fig. 10A). Summarizing these observations in granular zircon, three stages of crystallinity were documented (Fig. 7D, E): amorphous or with only a few nanocrystals of zircon embedded; mosaic crystal, which is formed from zircon nanocrystals misoriented to each other and is shown by patchy diffraction contrast; and recrystallized zircon with distinct diffraction contrast replacing zircon mosaic crystals (Fig. 7D, E). Spherical and elongated inclusions of Zr-oxide (< 1 μm) (Figs. 6A, B; 7A, B) occur enclosed within zircon granules, together with enrichment of Y in zircon (Supplementary file). Triple junctions between the granules are either empty space
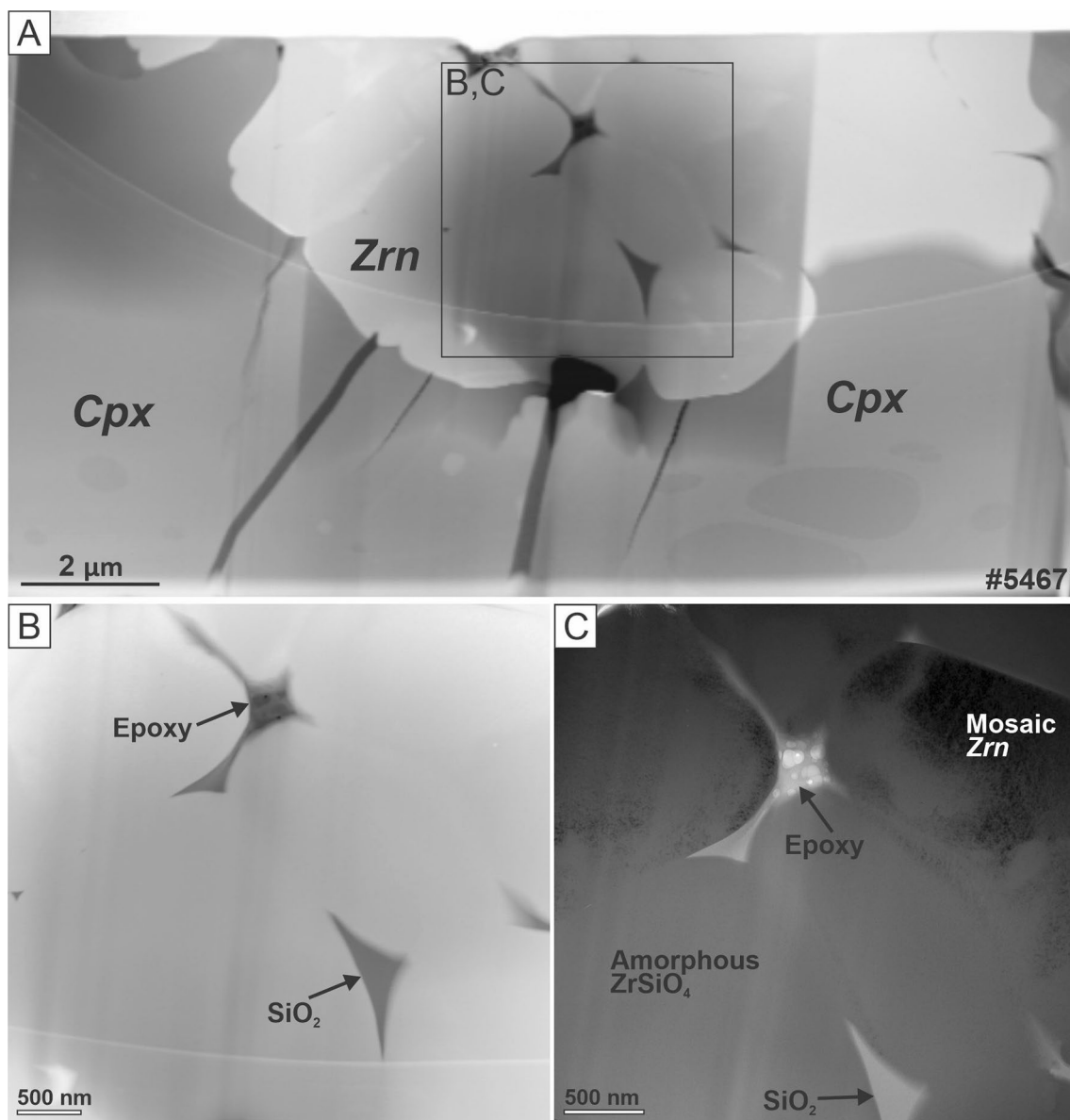

Fig. 5 A HAADF image. An overview of triple junctions in a granular zircon; **B** HAADF image. Simple triple junction with visible interfaces between zircon granules; **C** BF image of a triple junction filled with silica melt containing spherical inclusions of epoxy, foil # 5467
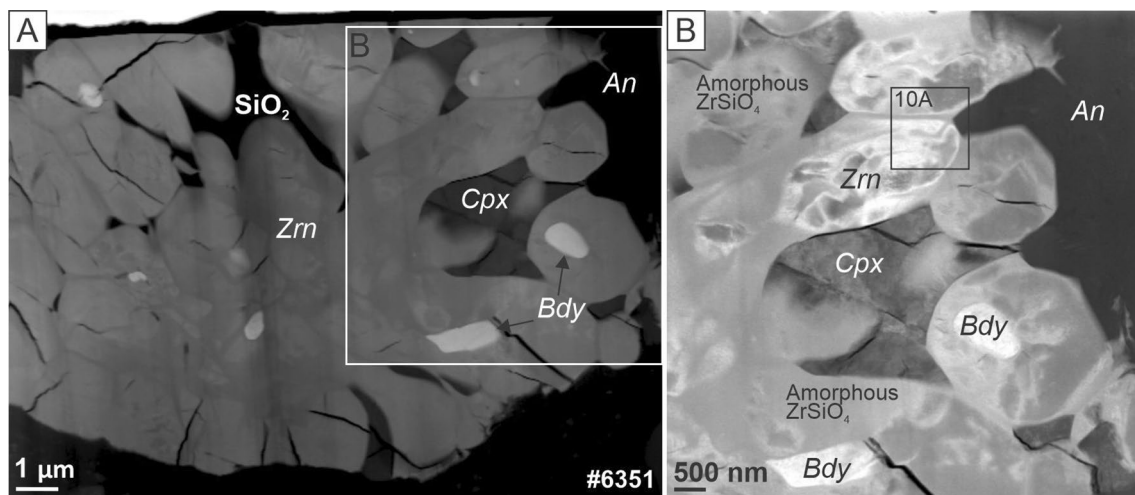
Fig. 6 **A** The HAADF Z-contrast image of zircon in 1D; #6351. **B** The HAADF diffraction contrast + Z-contrast image showing distribution of fractures and various phases, such as zircon (Zrn), clinopyroxene (Cpx), SiO_2, baddeleyite (Bdy) and anorthite (An); foil #6351

filled with epoxy resin containing bubbles, clinopyroxene (Fig. 6A) or are filled with amorphous silica-rich glass containing minor Mg and Fe or Al and K (Figs. 5B, 7C). Particles with bright contrast in Fig. 6A are baddeleyite inclusions that are ≤ 1 µm in size showing polysynthetic twinning (Fig. 7E). Open radial fractures are common in the outer parts of granular zircon aggregates. Fractures are also observed in the surrounding silicates.

Zircon–baddeleyite intergrowth

Foil #6354, #6355; thin Section 15455,27

These samples contain irregular intergrowth composed of relatively large baddeleyite cores (monoclinic ZrO_2 was confirmed by electron diffraction) enriched in Y and Ti (Supplementary file), in contact with a granular zircon rim and is hosted by anorthite (Fig. 1G, H). The aggregates studied here are approximately 100×60 µm (#6354) and contain inclusions of merrillite and possibly armalcolite, and 70×20 µm (#6355), where zircon is locally present as granules with triple junctions. The interface between baddeleyite and zircon rim (center in Fig. 8A), and between zircon rim and surrounding anorthite (the darkest contrast, right) is irregular and cuspate–lobate, locally expressed as an open fracture (Fig. 8B). The left part in Fig. 8A shows interfingering of zircon with baddeleyite in the center of this aggregate. Intensive twinning characterizes baddeleyite internal structure in both specimens (Fig. 8A). The bright contrasts between the twin lamellae indicates locally high dislocation densities. Baddeleyite contains multiple inclusions of Nb- and Cr-bearing TiO_2 (Fig. 9A, C). In most cases, there are tetragonal (rutile); however, in some cases monoclinic structure of crystals indicates for the possible presence of

akaogiite. Due to the small size of such crystals, it is impossible to determine them unequivocally. Therefore, all TiO_2 inclusions in the next part of the paper are called 'rutile', due to the clear identification of bigger grains. Rutile inclusions are round or elliptical (Fig. 9A) with curved interfaces between rutile and baddeleyite. Figure 9C shows a bright-field image with an elliptical rutile crystal and triangular-shaped intrusions of rutile along baddeleyite with cuspate-lobate boundaries.

In some cases, ZrO_2 is present as nanometre-sized (< 100 nm) isolated spheres or drop-shaped grains within zircon granules. The ZrO_2 nanospheres have a cubic crystal structure (diffraction pattern in Fig. 9B) that distinguishes them from the larger, 10–20 µm-size grains of monoclinic ZrO_2 identified as baddeleyite. Additionally, ZrO_2 in this study form a tetragonal crystal structure. At triple junctions of zircon granules and within the baddeleyite, small inclusions (< 100 nm) of FeS and FeNi were observed. In one location, a FeNi grain of 100 nm in length is hosted by a slightly larger FeS crystal (Fig. 9D). Because of the small size of the intergrowth, the spectrum shows a mixed analysis (Fig. 9F). Another nanometre-sized crystal of FeNi (97.05 at. % Fe, 2.95 at. % Ni) was observed in granular zircon and is shown in Fig. 9E. Similar inclusions are found elsewhere in the main baddeleyite mass.

The zircon rim has a very weakly developed columnar internal structure, seemingly radiating from baddeleyite (Fig. 8). The different grey scale within the zircon rim (Fig. 8A) is indicative of locally variable density, where some volumes of the grain are amorphous (darkest parts), and the brighter are mosaic crystal domains (assembled from zircon nanocrystals). The mosaic crystal domains have sub-rounded or angular shape forming "islands" separated from each other by amorphous domains that are interconnected
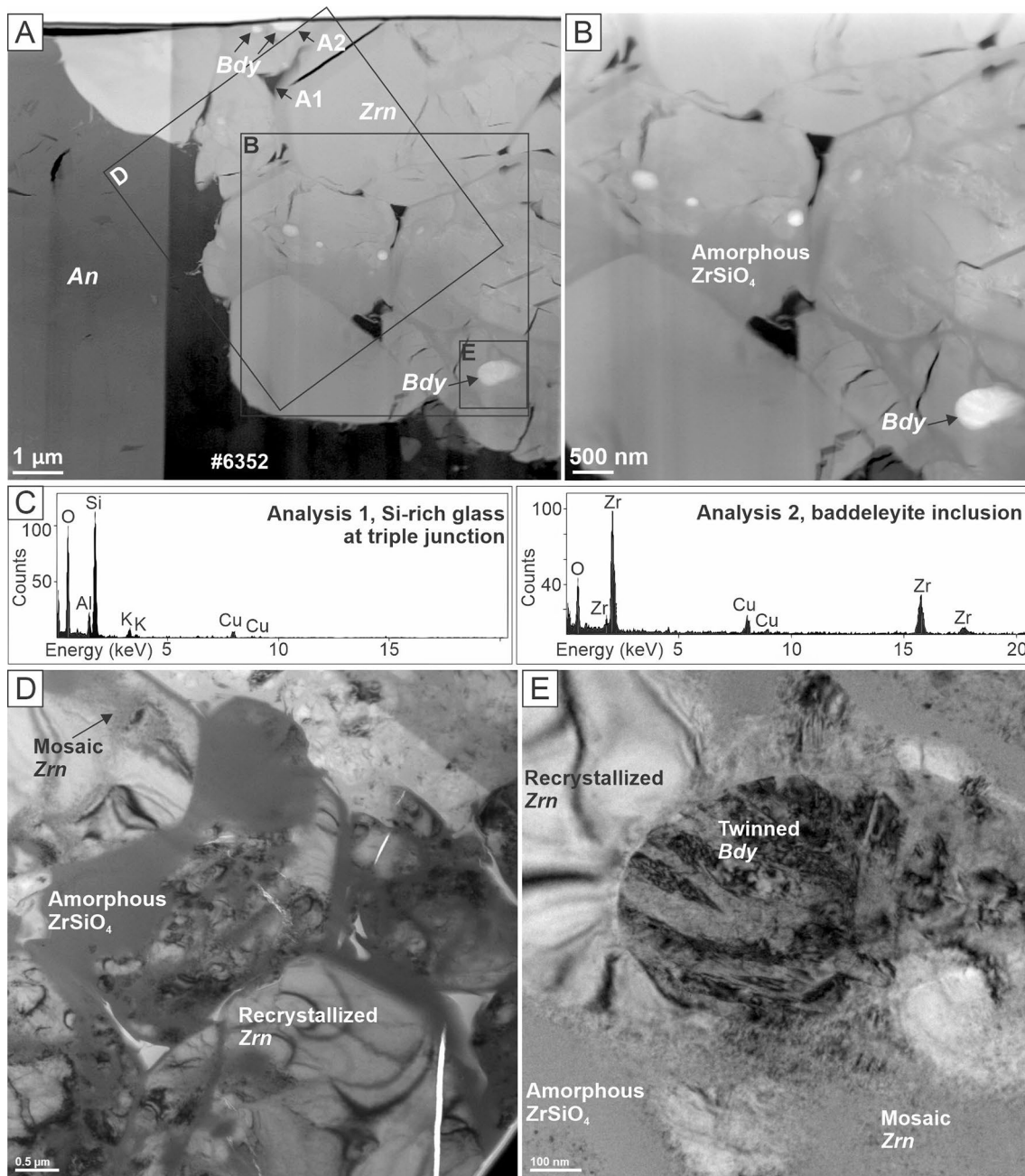
Fig. 7 A The HAADF Z-contrast image of zircon in 1D; #5362. **B** Inclusions of baddeleyite in zircon and trapped silica together with a fracture. Squares show areas of analysis presented in figure **C**; **D**, **E** three stages of zircon crystallinity: amorphous or with only a few nanocrystals of zircon embedded; mosaic crystal and recrystallized zircon; foil #6352

into a web-like texture (Fig. 8A, B). In low magnification TEM bright-field images, zircon usually shows homogeneous grey contrast (e.g., Figure 3B) with diffraction contrast absent, typical for an amorphous state of $ZrSiO_4$. However, at higher magnification, the grey areas reveal dark nanometre-sized patches with diffraction contrast (Fig. 10). The dark diffraction contrast patches in these volumes represent nanocrystalline zircon embedded in an amorphous matrix with zircon composition (light grey). Amorphous areas almost free of zircon nanocrystals (i.e., no dark diffraction contrast patches) and areas with varying density of nanocrystals are observed (Fig. 10). Thus, the studied zircon is composed of amorphous domains that gradually change to partially crystalline mosaic domains with individual zircon nanocrystals that are slightly misoriented from each other. It is worth to note that in high-resolution lattice fringe images
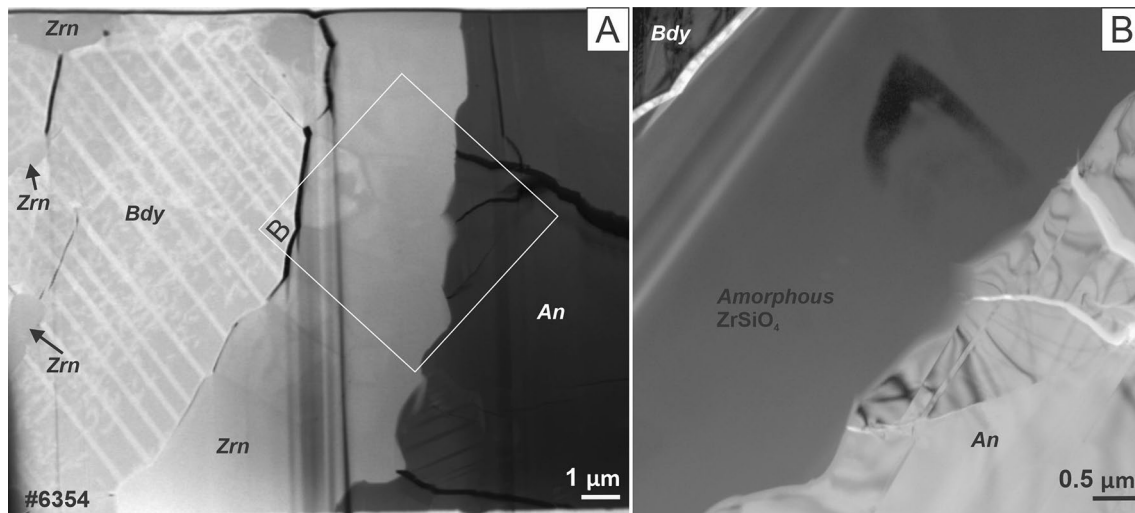
Fig. 8 A The overview HAADF Z-contrast image showing: twin lamellae of baddeleyite (brightest Z-contrast) with few patches of zircon intergrown (left part); zircon displaying columnar features (central part); and anorthite (dark contrast on the right part); **B** bright field (BF) image of amorphous part of the ZrSiO$_4$ with dark triangu-lar-shaped patchy diffraction contrast (mosaic crystal of zircon) and anorthite matrix; foil #6354. Note that on the HAADF image, anorthite has darkest contrast and, on the BF image, it has brightest contrast

of mosaic crystals, there is no silicate melt on the interfaces between the individual nanocrystals. The recrystallized part of zircon grows on expense of the mosaic crystal and has partially replaced it (Fig. 10A). Matrix anorthite reveals low dislocation density, numerous twins and low-angle grain boundaries (Fig. 8B, right-hand side).

Summary of key observations

- Four types of zircon occurrences were documented:

  (1) Anhedral grains with planar fractures, possibly mineral clasts, in the brecciated matrix (Figs. 1A; 2). Planar fractures are associated with displacements visible at the grain surface (Fig. 2).

  (2) Subhedral, conchoidal zircon on grain boundaries between silicates (Figs. 1B, C; 3; 4, see also Supplementary figure S3 in Vanderliek et al., 2021a). The zircon grains comprise partially amorphous and partially mosaic nanocrystal domains.

  (3) Granular aggregates, with or without inclusions of ZrO$_2$ (Figs. 1D, E, F; 5, 6, 7, 10); zircon granules are composed of partially amorphous, partially mosaic nanocrystals and partially recrystallized domains.

  (4) Irregular overgrowth and intergrowth of zircon with baddeleyite (Figs. 1G, H; 7, 8, 9) in host anorthite. Zircon aggregates form mosaic

  nanocrystals surrounded by partially amorphous parts.

- Zr-oxide occurs in three different crystallographic forms. Larger ZrO$_2$ grains are commonly present as monoclinic baddeleyite; however, small (< 100 nm) inclusions of ZrO$_2$ in zircon have cubic crystal structure (Fig. 9). Tetragonal ZrO$_2$ is also present. Features characteristic of baddeleyite are polysynthetic twin lamellae and high dislocation densities (Figs. 8A; 7E).

- Zircon usually displays patchy diffraction contrast due to the presence of nanocrystalline zircon. Nanocrystals of zircon are occasionally present as isolated islands in amorphous parts of the grain or can be assembled due to surface charge forces forming a mosaic crystal. Nanocrystals building a mosaic crystal are slightly misoriented with respect to each other (Fig. 10), they can be partially or completely recrystallized into crystalline grain with long-range order (Fig. 10B).

- In granular zircon aggregates, granules are euhedral with different orientation (#5467, Fig. 5; #6351, Fig. 6; #6352, Fig. 7) and different degree of crystallinity, either with cores of the granules being amorphous and rims forming either mosaic crystals or recrystallized zircon (#5467); or the opposite (#6351 and #6352), crystalline cores and amorphous rims of the granules. Granular aggregates are often fractured.

- Triple junctions between the zircon granules are either empty or filled with amorphous SiO$_2$ (Figs. 5; 6), sub-
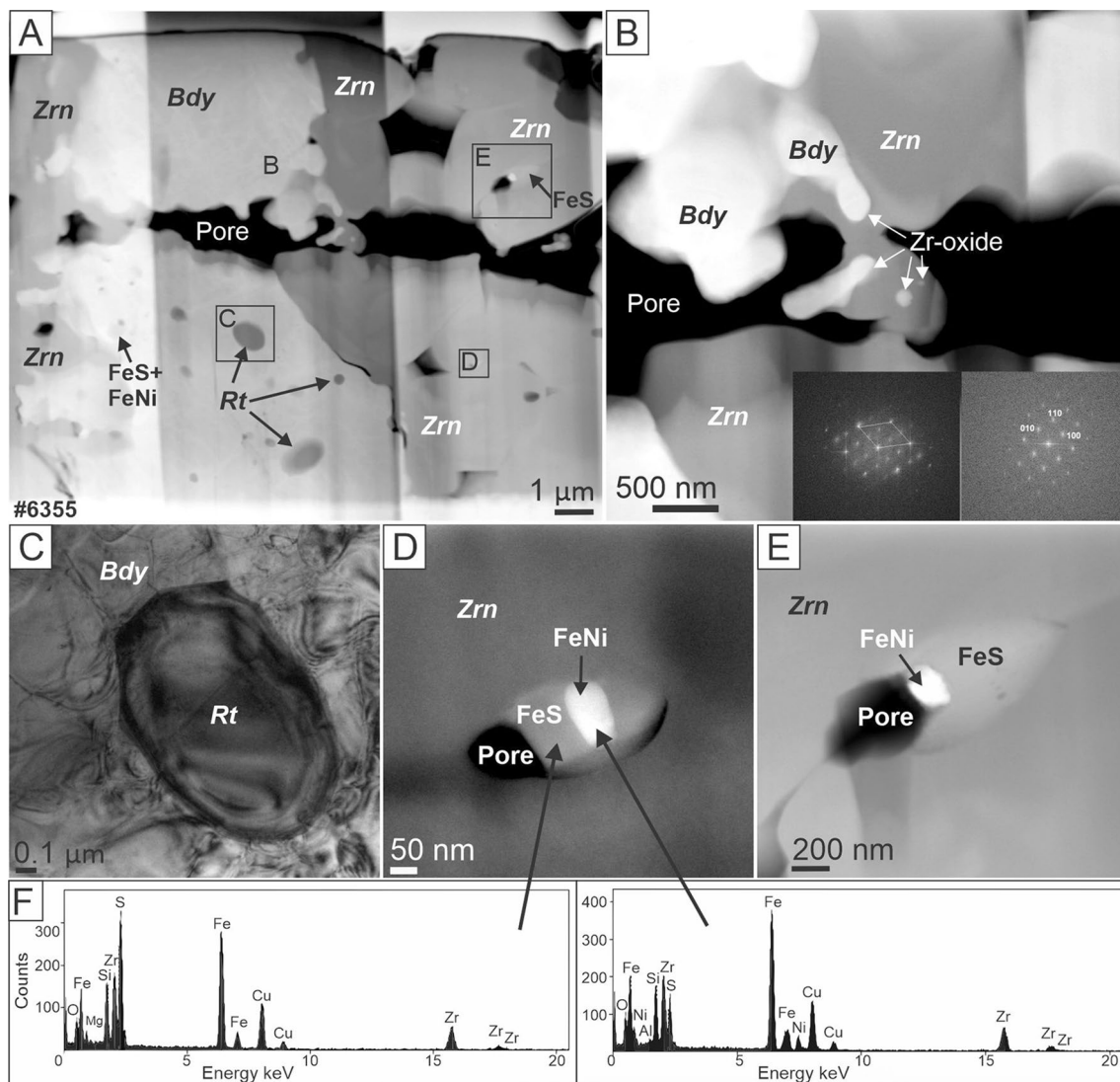
Fig. 9 **A**, **B** The overview HAADF TEM image showing the intergrowth of zircon (Zrn) and monoclinic Zr-oxide (baddeleyite; Bdy) together with a large open pore space. Baddeleyite contains inclusions of rounded rutile (Rt); **B** detailed HAADF TEM image with droplets of Zr-oxide (zirconia) in zircon, insets showing FFT patterns of cubic ZrO_2 (zirconia) inclusions; **C** BF image of rutile entrapped in the crystallizing baddeleyite; #6355. **D**, **E** HAADF image of inclusions of FeS and FeNi at triple junctions of zircon crystals. The boxes represent the locations of the corresponding analysis; **F** EDS spectra of FeS and FeNi inclusions in zircon, shown in **D**; foil #6355

micron-size FeNi alloys and FeS crystals (Fig. 9), as well as clinopyroxene (Fig. 6).

- No Pb nanospheres were observed in zircon from analyzed samples.
- Host anorthite shows low dislocation density and numerous twins and low-angle grain boundaries (Fig. 8B).

Discussion

In the studied samples, we observed various micro-structures, some of them are known from zircon in terrestrial impactites and indicate shock metamorphism or post-shock deformation and annealing processes. Here we focus on the most complicated and unusual features in zircon and discuss them in the light of published U–Pb geochronology.

Brittle deformation features

Planar fractures (PFs) are observed in a zircon clast (foil #6353). In igneous or metamorphic terrestrial zircons, PFs do not occur under normal crustal conditions, because zircon has only imperfect {110} or poor {111} cleavage (Deer et al. 1997). However, PFs are common in zircon from impactites (e.g., Timms et al. 2012; Kovaleva and Habler 2019; Wittmann et al. 2021). Fractures
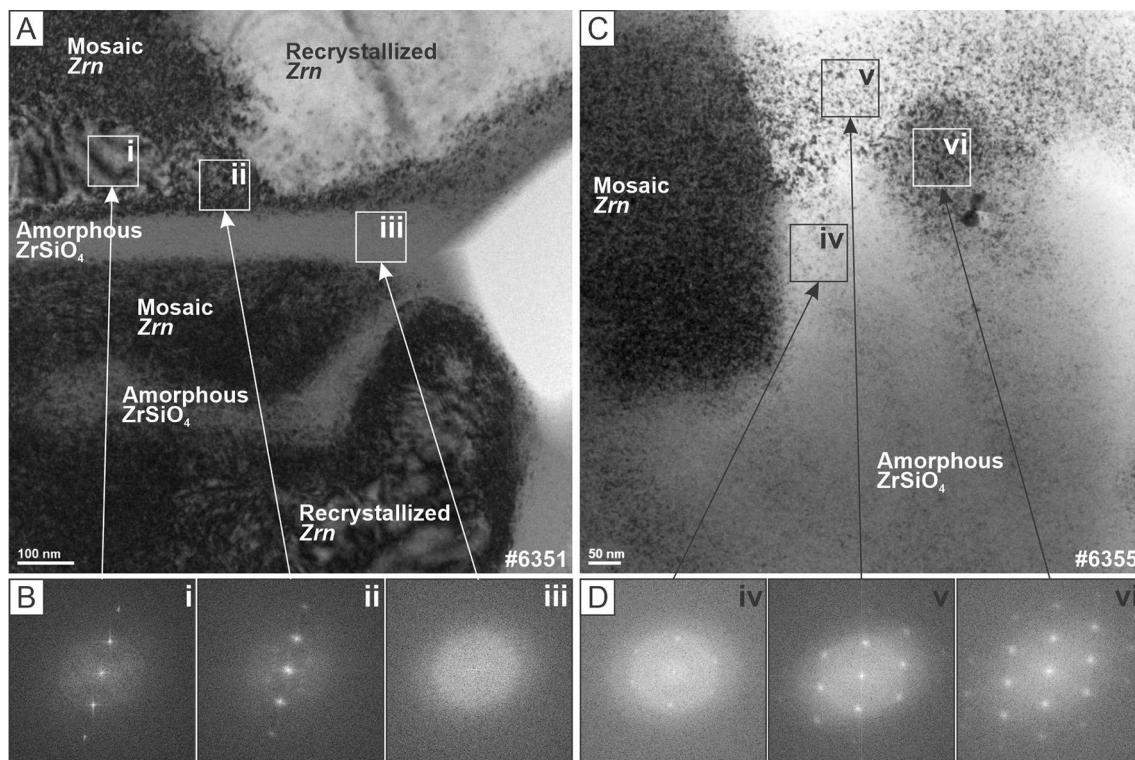
Fig. 10 **A**, **C** The BF image of zircon showing nanometre-sized patchy contrast with patches of dark diffraction contrast representing crystalline state of zircon. **A** Granular zircon aggregate, foil #6351. Two grains of zircon with different crystal orientation separated by a layer of amorphous $ZrSiO_4$ ca. 100 nm wide. B. Zircon granular rim, foil #6355. In both images dark diffraction contrast patches represent nanocrystalline zircon embedded in an amorphous matrix of zircon composition (light grey). Amorphous areas are almost free of zircon nanocrystals (i.e., no dark diffraction contrast patches) and areas with higher density of dark contrast patches indicating more nanocrystals of zircon. Areas of high-resolution lattice fringe images acquired are shown as (i), (ii), (iii), (iv), (v), (vi). **B**, **D** High-resolution lattice fringe images acquired from several locations and the related diffraction patterns obtained by FFT showing varying crystallinity while the zone axis orientation remains the same, indicating a single crystal. (i) Sharp diffraction spots of mosaic part of zircon with the same orientation as (ii); (ii) the recrystallized part of the zircon grows on expense of the mosaic crystals and has partially replaced it; (iii), (iv) diffraction patterns with broad and diffuse diffraction spots together with strong diffuse scattering intensity in the background (bright diffuse ring) that indicates amorphous material; (v) slightly sharper diffraction spots and less diffuse scattering intensity from the amorphous material, indicating more nanocrystals of zircon; (vi) crystal with incipient mosaic nano-structure

forming nm-scale displacements along the grain boundary (Fig. 2B) indicate shearing. The PFs occur during mild shock pressures (< 20 GPa, Timms et al. 2017), as high shear stresses affect the grain during impact process (Timms et al. 2012; Kovaleva and Habler 2019).

Non-planar microfractures are also common in zircon grains of various settings (Figs. 3; 4A, 8A; 6; 7; Vanderliek et al. 2021a) and could be caused by contraction during cooling, for instance, if crystallization from shock-related melt took place (e.g., Figures 8A; 6). Alternatively, similar to PFs, brittle deformation may have occurred during the displacement of ejecta. Other fractures are likely to have formed due to expansion of amorphous domains, because these fractures preferentially occur in crystalline domains that surround the amorphous ones (Figs. 1B, C, 4, 6, 7A, B). The mechanisms of amorphization are discussed below.

Origin of granular zircon and its inclusions

Shock-induced decomposition and back reaction

Granular zircon with or without ZrO_2 and amorphous SiO_2-rich glass is common in terrestrial impactites (e.g., Cavosie et al. 2018a, b; Kovaleva et al. 2021) and also was observed in lunar impactites (Crow et al. 2017; Grange et al. 2009; 2013a; Vanderliek et al. 2021a; Wentworth and McKay 1991; Zhang et al. 2011). Granular zircon with inclusions of ZrO_2 and amorphous SiO_2 was described as a product of shock-induced incongruent melting of zircon, and subsequent crystallization from melt (Kovaleva et al. 2021).

Zircon granules in such aggregates are usually mosaic crystals composed of nanocrystals slightly misoriented from each other (e.g., Fig. 5C), pointing at rapid crystallization from melt (amorphous domains). At T > 1687 °C (assuming

equilibrium conditions), zircon decomposes into liquid SiO_2 and solid ZrO_2, either monoclinic, tetragonal (> 1673 °C), or cubic (> 2370 °C). At a T > 2250 °C, both oxides exist as immiscible melts, and > 2500 °C zircon exist as a homogenous liquid (Kaiser et al. 2008). It must be emphasized that the heterogeneous textures in the impactites suggest that the phase transformations reflect disequilibrium processes and temperatures derived from phase equilibrium processes might not be relevant for highly dynamic shock environments. For example, under certain shock-loading conditions, zircon directly produces a homogenous liquid without decomposition into oxides (Takagi et al. 2022).

Upon cooling, the two oxides began to back-react, forming new zircon grains, which often contain relic inclusions of ZrO_2 and amorphous SiO_2. Thus, granular aggregates composed of individual grains < 3 μm size (foils #6355 (rim), #5467, #6351, #6352; Figs. 1H, 5, 6, 7, 9A) likely have formed from shock-induced remelting of pre-existing zircon of uncertain origin. It is possible that Ti originally present in high-temperature Zr-silicate or ZrO_2 'exsolved' upon quenching and formed TiO_2 (Fig. 9C). Further constraints on the origin of the precursors of granular zircon will be discussed further.

ZrO_2 inclusions and their significance

Spherical nano-inclusions of Zr-oxide represent monoclinic (baddeleyite), tetragonal and cubic (zirconia) Zr-oxide phase. In foil #6355, several ZrO_2 nanospheres have a cubic crystal structure. This observation is the first direct report of cubic zirconia (Fig. 9B inset) in lunar impactites.

Previously, the original presence of cubic zirconia in terrestrial impactites was indirectly inferred from crystallographic orientations of baddeleyite reaction rims surrounding zircons (Timms et al. 2017). Similarly, White et al. (2020) applied EBSD and determined a cubic precursor structure in a large baddeleyite grain from the lunar troctolite 76235. Recently, cubic ZrO_2 was directly observed and documented in granular zircon from the Vredefort impact structure (Kovaleva et al. 2021). The spherical shapes of nanocrystalline zirconia inclusions might indicate that they have nucleated and grown from a zirconia melt droplet, which requires a temperature exceeding 2715 °C at equilibrium conditions (Kaiser et al. 2008). The cubic structure was preserved because the spheres are nanocrystalline (Gleiter 1989). It has been shown in experimental studies that Fe similarly does not experience phase transformation in nanoparticles. Usually, Fe transforms from high-temperature body-centered cubic structure (bcc) to low-temperature face-centered cubic structure (fcc) at 911 °C. However, in a nanocrystalline state of Fe, the reversed transformation upon cooling is inhibited and the high-temperature fcc structure is preserved (Gleiter 1989). By analogy, phase transition

of ZrO_2 from cubic to monoclinic crystal structure in the smallest inclusions could be prevented. The spherical shape of inclusions (Fig. 3B) and common association with SiO_2 glass inclusions further indicate that the capture of these inclusions occurs in liquid state and probably at temperatures above 2250 °C, when ZrO_2 melt and SiO_2 melt are immiscible (Kaiser et al. 2008; Kovaleva et al. 2021).

Origin of large baddeleyites and their micro-structures

The occurrence of baddeleyite as relatively large single grains (here termed "large baddeleyite", Figs. 1G, H, 8A) in lithologies of the lunar Mg suite has been already documented (e.g., Lunar Sample Compendium; Meyer 2005). However, its origin remains uncertain and debated (Grange et al. 2009; White et al. 2020). Baddeleyite occurs as a primary igneous mineral in SiO_2 undersaturated magmatic rocks on Earth (Heaman and LeCheminant 1993) and in Martian meteorites (White et al. 2019; Zhou et al. 2013). In breccia 15455, baddeleyite is restricted to the anorthositic norite lithology and baddeleyite grains preferentially occur with evolved intercumulus diopside–SiO_2 bearing domains. This mode of occurrence may imply that it represents a primary igneous mineral. However, like other lunar norites (e.g., from the Apollo 17 landing site), 15455 contains free SiO_2 (Vanderliek et al. 2021a) and therefore SiO_2 is oversaturated, almost certainly a primary igneous feature of the norites. Therefore, because of high a_{SiO2} in the parent magma, zircon should have been the primary magmatic Zr mineral and not baddeleyite. Because of the coherent nature of the norite in 15455,27 and ,28 and the preferred association with evolved mineral assemblages in the SiO_2–diopside-rich domains, it is difficult to conceive that baddeleyite and their zircon rims were mixed in as clast material that originated in other rocks. There is also no textural evidence that the present phase assemblages might represent clasts, given the interlocked and cuspate shape of the mineral aggregates. It must be emphasized that both foils of 15455 sample (#6354 and #6355) have strongly rounded interfaces of baddeleyite/zircon and zircon/matrix silicate. In some areas, zircon protrudes into the matrix silicate (Fig. 1G) or extends along matrix silicate grain boundaries (Fig. 1H). Such micro-structures would be expected to develop within unmixed melt systems (silicate and oxide melt).

Tetragonal ZrO_2 could be a product of the decomposition of $ZrSiO_4$ (tetragonal zircon), which, in SiO_2 oversaturated environments occurs in impact melts and glasses at temperatures exceeding 1676 °C (e.g., Heaman and LeCheminant 1993; Kaiser et al. 2008; Timms et al. 2017). However, the common mode of occurrence of ZrO_2 as breakdown product of zircon is as sub-micron size, tear-drop or vermicular-shaped grains, surrounded by silica glass or zircon (Fig. 6A,

Fig. 7 this work; Crow et al. 2017; Grange et al. 2013b; Kovaleva et al. 2021). Thus, large baddeleyites might have a different origin, for instance by structural conversion from cubic ZrO_2 during rapid cooling. White et al. (2020) used electron backscattered diffraction to show that a large monoclinic baddeleyite in the pristine lunar troctolite 76565 had a cubic precursor structure, implying very high temperatures > 2370 °C (Kaiser et al. 2008); thus, the precursor phase could have formed together with the cumulate assemblage from a superheated impact melt sheet. Baddeleyites in pristine norites such as 15455 may have a similar origin; however, this will require confirmation by additional crystallographic studies.

It has been suggested that baddeleyite can serve as an indicator of shock deformation, if it was present before the impact event(s) (e.g., White et al. 2018). Dense twinning, dislocations and fractures observed in large baddeleyite grains (Fig. 8) are typical features occurring due to the phase transformation of tetragonal Zr-oxide to the monoclinic crystal structure below 1200 °C (Telle et al. 2015). Such transformation is accompanied by a positive volume change of approx. 5 vol% associated with a transformation strain (Chevalier et al. 2009). The tetragonal to monoclinic phase transformation is a martensitic phase transformation and was already documented in the Zr-oxide ceramic literature (Chevalier et al. 2009). Therefore, twinning and dislocations in baddeleyite are not necessarily shock-induced features.

Zircon rims surrounding large baddeleyite grains

Large baddeleyites in the anorthositic norite lithology of breccia 15455 (sections ,27 ,28) are surrounded by up to 20 μm-thick rims of zircon (Fig. 1A, B). Both minerals are in contact with phosphates; however, zircon shields the baddeleyite and prevents direct contact of baddeleyite with surrounding silicate grains (diopside, silica, plagioclase, orthopyroxene). Grange et al. (2009; 2013b) reported similar intergrowth from Apollo 15 and 17 impact breccias. Because some of the zircons and baddeleyites have been dated (Vanderliek et al. 2021a, b), it is important to understand their origin. Davidson and van Breemen (1988) have documented polycrystalline columnar rims of zircon around the single-crystal baddeleyite cores in terrestrial metagabbro from the Ontario province in Canada. Those textures are nearly identical to the wide columnar zircon rims in Fig. 8 (foil #6354). The authors concluded that the zircon rims formed around primary magmatic baddeleyite as a result of increased silica activity during metamorphism, some 125 Ma years after magmatic crystallization of the baddeleyite. Similar conclusions were derived by Wingate et al. (1998) for polycrystalline zircon overgrowths on baddeleyite from mafic metaigneous rocks from Australia. According to Wingate et al. (1998), zircon

rims around baddeleyite point at the reaction between ZrO_2 and free silica. In terrestrial rocks, such reactions may occur during metamorphism and associated metasomatism or hydrothermal alteration, and the zircon rims become thicker with an increase of metamorphic degree (Heaman and LeCheminant 1993). However, in the volatile element poor lunar crust, metasomatic processes involving Si-bearing aqueous fluids are unknown.

Even though there was no tectonic metamorphism and related metasomatism on the Moon, the existence of the large lunar basins, large volumes of ejecta and impact melt suggest that shock metamorphism and heating during impacts must have been very intense. Grange et al. (2009; 2013b) also reported zircon coronas around baddeleyite in lunar breccias and interpreted these as a result of reaction of baddeleyite grains with surrounding silica-rich melt that were mixed together during brecciation. The relatively coherent igneous nature of the noritic fragments of breccia in Sections 15455,27 and ,28 and the preservation of intercumulus domains containing diopside, silica, Zr minerals and phosphates rule out mechanical entrainment of Zr phases during brecciation events. Thus, localized shock-related reaction of the large baddeleyite with nearby silica oversaturated melt produced by localized shock heating of primary SiO_2–feldspar-bearing mineral assemblages is the most viable zircon rim formation mechanism in the present case. Thick zircon rims such as in 15455 may reflect more intense or more prolonged shock heating than thin zircon rims reported from relatively small impact events that occurred late in lunar history (Darling et al. 2016; Grange et al. 2013b; Moser et al. 2013). Localized melting was reported from other lunar samples (Crow et al. 2019). Cuspate and irregular boundaries between zircon and surrounding plagioclase, and zircon and baddeleyite indicate textural disequilibrium (Figs. 1G, H, 8, 9) and are consistent with localized reactions or with unmixed melts. Localized melting processes would imply disequilibrium and very high temperatures, or early crystallized cubic ZrO_2 would not have formed.

Grange et al. (2009) noted that in their samples, zircon rim around baddeleyite shows a granular texture and contains small inclusions of ZrO_2. This is in agreement with the original presence of unmixed oxide and silicate melts. In our sample 15455,28 foil #6355, there is a textural evidence for at least two formation stages: first, the formation of a thick zircon rim around baddeleyite (Figs. 1G, H, 8), then later, lower-temperature shock deformation of the baddeleyite–zircon aggregate with incipient formation of zircon granules with nanocrystalline–amorphous domains, inclusions of ZrO_2 within zircon (a result of zircon decomposition), and highly irregular boundaries associated with empty pore space (Fig. 9).

Origin of amorphous and recrystallized domains in zircons

Amorphous, mosaic and recrystallised domains in studied zircon occur in close relationships with each other and transition into each other (Fig. 10).

Mosaic domains vs metamict domains

Mosaic domains are domains that are composed of nm-sized crystals that are slightly misoriented from one another (Fig. 4). Mosaic domains may be a result of local crystallization from a melt phase commencing in a nanocrystalline state (e.g., Kusiak et al. 2015; Kovaleva et al. 2021), and their pervasive presence (Figs. 4; 5C; 7D; 9; 10) indicates (re)crystallization of many of the observed lunar zircons from amorphous $ZrSiO_4$. Diffraction patterns of observed mosaic crystals are broadened and smeared out without preferred orientation (Fig. 10C iii, D iv).

Dark nanometre-sized patches visible in foil #6353 (Fig. 2B) represent different types of nanocrystalline mosaic domains that can be attributed to coherent scattering units, typical for irradiation-damaged (metamict) zircon. They represent islands of the original zircon crystal lattice that was affected by irradiation damage, which produced nanometre-sized islands of SiO_4 tetrahedra networks and Zr-oxide in a slightly distorted matrix of the original zircon (Anderson et al. 2008; Nasdala et al. 1995, 2009). The difference in volume between such metamict areas and the original zircon results in distortion of the zircon crystal lattice. This is evident from the electron diffraction patterns (Fig. 10), which show a distortion of the diffraction spots depending on the orientation of the crystal and the anisotropy of the elastic constants in zircon (Anderson et al. 2008; Nasdala et al. 1995, 2009). Coherent scattering units associated with metamict zircon are different from mosaic crystals of granular aggregates (Fig. 10), which show smeared out and broadened diffraction spots due to slight misorientation of the individual nanocrystals (Fig. 10C). Thus, the apparent "mosaicism" of grain #6353 is a true radiation damage, not observed in the other foils. Overall, these observations fit the nature of this grain as a mineral clast and may hint at a primary igneous origin, whereas, in other studied zircons, such original features were destroyed by impact-related amorphization and recrystallization processes.

Amorphous domains in zircon

Amorphous domains in terrestrial zircon often reflect the initial variability of U and Th in the grains. Metamictization of the crystal lattice, leading to amorphization occurs because of enhanced destruction of the lattice by alpha decay in U–Th-rich domains, which follow igneous growth zoning and often being marked by a presence of Pb nanospheres (e.g., Kusiak et al. 2015; Lyon et al. 2019). Amorphous domains in our samples do not follow growth zoning (which, in most cases, is absent). Darling et al. (2016) described shock-related amorphization of baddeleyite in shergottite. On the other hand, amorphization due to solar irradiation or to the impact-generated vapor condensation and sputter deposition is often attributed to the rims of grains that were exposed on the lunar surface (Keller et al. 2021; Wentworth et al. 1999).

Pidgeon et al. (2018) and Crow et al. (2019) reported a lunar zircon grain with amorphous parts, suggesting radiation damage or shock metamorphism. Grange et al. (2013b) noted an irregular network of amorphous domains that is surrounding crystalline islands in 'pomegranate' zircon grain. The authors noted that the distribution of these amorphous domains is highly irregular and is not consistent with primary growth zoning. Therefore, the loss of crystallinity could not have been caused by simple metamictization of primary igneous zircon. Grange et al. (2013b) conclude that the amorphous domains are diaplectic glass, created by a shock wave. Similarly, the experimental results by Gucsik et al. (2002, 2004) suggest that shock propagation damages the zircon lattice similar to radiation-induced metamictization.

Results of the present study demonstrate that amorphous domains in zircon from lunar impactites are a much more widespread phenomenon than was noted before. Grange et al. (2013b) only observed amorphous domains in two grains ("pomegranate" and "propeller") from a lunar impactite, while in our samples, we observed them in seven out of eight studied grains (Figs. 3, 4, 5, 6, 7, 8, 10). Similar to the case described by Grange et al. (2013b), shapes of amorphous zircon domains do not follow any other structures such as concentric zones, grain boundaries or fractures. Amorphization in lunar zircon grains is not related to any primary features as, for instance, is the case in terrestrial radiation-damaged zircons. Amorphous zircon domains represent a diaplectic $ZrSiO_4$ glass which was a product of high-pressure shock events that occurred after the grains were formed.

Nanocrystals of recrystallized domains in zircon

The numerous and slightly misoriented nanocrystals of mosaic zircon domains form low-angle grain boundaries, and thus increase the inner energy of the system. Area (iv) in Fig. 10C represents a well-crystallized zircon domain where the mosaic lattice has been completely replaced by recrystallized zircon, thus reducing the inner energy of the crystal. The corresponding diffraction pattern (Fig. 10D) shows sharp diffraction spots with the same crystal orientation as

the mosaic domain. Most probably, zircon grains originally were fully crystallized and then partially transformed into amorphous material by the very short-term shock event. Recrystallized domains present in amorphous material (Figs. 7D, E; 10C and Grange et al. 2013b) likely formed due to local lattice recovery during the short-term post-shock thermal pulse.

In the study of Grange et al. (2013b), such textural domains were considered to be important because they can be large enough to be dated and involved in resetting of the U–Pb system. Recrystallized domains were also observed by Kovaleva et al. (2021) in zircon granules from Vredefort impact structure, crystallized from shock-induced melt. However, this recrystallization was not caused by later impacts, but more likely by prolonged heating of the zircon entrapped in the impact melt dike.

The significance of micro-structures for the interpretation of U–Pb ages of zircon

The great variety of nano- and micro-structures in different types of zircons from the lunar breccias stands in stark contrast to the relatively uniform distribution of $^{207}Pb/^{206}Pb$ ages from zircons (and baddeleyite) in the studied sections (Vanderliek et al. 2021a, b). In 15455, 27 and 28, most zircons are concordant with only a few being analytical spots being reversely discordant. The $^{207}Pb/^{206}Pb$ ages range between 4210 and 4201 Ma in Section 27 and between 4200 and 4154 Ma in Section 28. The youngest and oldest of the zircon ages can be resolved and thus must reflect different heating events. The 4220–4210 Ma event is also common in phosphates and some other zircons in various breccias from the Apollo 14, 15, 16 and 17 landing sites and, thus, may represent a major basin-forming impact (Cernok et al. 2021; Crow et al. 2017; Nemchin et al. 2021; Norman and Nemchin 2014; Vanderliek et al. 2021a). The slightly younger $^{207}Pb/^{206}Pb$ age near ~4150 Ma reflects one or several later heating events that could have led either to complete or minor partial Pb loss. For instance, minor Pb loss of 4.2 Ga zircon caused by heating processes associated with the Imbrium impact at ~3920 Ma (Nemchin et al. 2021; Snape et al. 2016) may have moved zircons along the concordia line toward younger ages.

To understand the role of the microstructural features in zircons of this study, we compare these features with the age record in the three breccias. Foil #6354 (Section 15455,27) was cut from a zircon–baddeleyite intergrowth that yielded $^{207}Pb/^{206}Pb$ zircon ages of 4204 ± 14 Ma and 4201 ± 15. Foil #6355 (Section 15455,28) is from a similar intergrowth, but yields a somewhat younger zircon age of 4168 ± 14 Ma. We note that, zircon rims in these aggregates are different: in foil #6354, we observe undistorted "columnar" rim structures composed of amorphous and partially amorphous domains

(Fig. 8), while in foil #6355 zircon, rim is granular and was subjected to secondary shock-related melting and recrystallization. Grange et al. (2013b) interpreted the U–Pb ages of recrystallized domains in zircon as reflecting the timing of later impacts. Thus, Pb loss postdating the 4200 Ma event could have been related to a later impact event that might have led to melting in the granular zircon rim of #6355. As the U–Pb ages of zircon in foil #6354 were not affected by further events, it is also possible that features documented in this grain had no influence on the ancient Pb mobilization and Pb is preserved in zircon despite various microstructures which occur here. The U–Pb ages combined with the textures indicate that the zircon granules crystallized at 4.2 Ga and retained their radiogenic Pb since then (Vanderliek et al. 2021a). In breccia 15455, Crow et al. (2017) reported large granular zircon aggregates with Pb–Pb ages of around 4.33 Ga. Hence, some of the granular zircons that yielded ages of 4.2 Ga may have replaced earlier impact-formed zircons. Despite the proximity of KREEP-rich melt veins presumably formed during the Imbrium impact (3.92 Ga, Snape et al. 2016; Nemchin et al. 2021), the U–Pb systems of the granular zircons were neither disturbed by the Imbrium impact, nor by later shock heating events.

Amorphous and nanocrystalline $ZrSiO_4$ domains occur in core and rim areas of granular neoblasts in foil #5467 (Section 15455,27; Fig. 5), yet ages of two spots are indistinguishable (4209 ± 9 and 4210 ± 14 Ma) and are similar to the older ages of zircon rims around baddeleyite cores. Granular zircon aggregates in clasts of the polymict breccia 67915 overall display similar behaviour. Zircon neoblasts display patchy to "veined" distribution of amorphous $ZrSiO_4$ in nanocrystalline to recrystallized zircon domains (#6351, #6352, Figs. 6, 7) with a $^{207}Pb/^{206}Pb$ zircon age of 4200 ± 61 Ma. Although sample 67915 is much more complex than 15455 and comprises a range of clast lithologies, it displays a relatively simple distribution of $^{207}Pb/^{206}Pb$ zircon ages ranging between 4241 and 4200 Ma in Section 67915,84 and between 4230 and 4200 Ma in Section 67915,76 (with most of the zircon data being concordant; Vanderliek et al. 2021a). The predominance of somewhat older ages in zircon clasts of the matrix (this work, Fig. 1A; and Fig. 4g in Vanderliek et al. 2021a) indicates that slightly older zircon fragments of uncertain provenance were mixed with zircons that recrystallized and lost most of their radiogenic Pb at 4210–4200 Ma.

A large impact event at ~4210 Ma is clearly indicated by the narrow zircon age distribution and other geochronological data on 67955 which was interpreted to have formed as igneous cumulate that crystallized in an impact melt sheet (Norman and Nemchin 2014; Norman et al. 2016; Vanderliek et al. 2021a). Conchoidal-shaped zircons (Fig. 1B, C) in this rock appear to have crystallized from interstitial melt pockets (Vanderliek et al. 2021a). These zircons also display

veined and patchy domains of mosaic zircon and ZrSiO$_4$ glass (Figs. 3, 4). Thus, the three breccias from different settings and a range of microscale to nanoscale textures show similar U–Pb age distributions with only minor spread toward slightly younger or older dates. In strong contrast, their phosphate ages (spreading from 4.2 to 3.9 Ga, Norman and Nemchin 2014; Nemchin et al. 2021; Vanderliek et al. 2021b) and the K–Ar dates of 3.9 Ga and younger (e.g., Fernandes et al. 2013; Norman 2009) clearly show that the rocks were affected by the Imbrium impact and subsequent heating events. Thus, it is surprising that the U–Pb system in zircon grains containing a range of amorphization, melting, and recrystallization features was not (or perhaps only slightly in case of a younger zircon in 15455,28, Fig. 9) affected by younger impact-related heating and shock events. We conclude that amorphization and variable nanoscale recrystallization ('mosaic zircon') as a result of later shock events did not lead to significant Pb loss in zircon, whatever its original formation history might have been (e.g., granular neoblasts, columnar zircon rims around large baddeleyites, single grain interstitial zircon, zircon clasts). Presumably, later shock and heating events were too transient for noticeable Pb loss to occur in the dry and reduced lunar environment.

Previous studies of terrestrial and lunar impactites have shown that granular recrystallization of pre-existing zircon and the formation of granular to vermicular zircon rims around baddeleyite typically lead to complete resetting of U–Pb systems in the recrystallized or new-formed zircons (Cavosie et al. 2015; Crow et al. 2017; Grange et al. 2009; 2013b; Kovaleva et al. 2021; Zhang et al. 2011). These results indicate that both small and large impact events may produce such textures. The greater energy delivered by basin-forming impacts leads to higher temperatures in impact melt sheets and more prolonged heating, which would be requirements for the decomposition of ZrSiO$_4$ (T > 1673 °C) and the formation of cubic ZrO$_2$ (T > 2370 °C) as documented here (Fig. 9 B inset) and in previous works (Kovaleva et al. 2021; Timms et al. 2017; White et al. 2020). On the early Moon, such conditions would then also favor destruction of previous generations of Zr minerals that may have formed by indigenous magmatism or previous large impact events. The prevalence of U–Pb ages around 4.2 Ga in recrystallized lunar zircons and various types of zircons that was formed by localized reaction with baddeleyite or crystallized from impact melt suggest high temperatures in the lunar crust during this time, presumably caused by basin-forming impacts. Such interpretation is in agreement with impact-related ages in zircon data going back to 4.33 Ga being rather scarce (Crow et al. 2017; Dürr et al. 2021; White et al. 2020).

The absence of Pb nanospheres (Kusiak et al. 2015) in the lunar zircon grains of the present study may also be an indication of more prolonged exposure to high temperatures. These conditions may have led to complete evaporation of radiogenic Pb that accumulated in Zr minerals or their precursor phases. The porous nature of some zircon–baddeleyite aggregates is consistent with this notion, although it is not clear which phases (i.e., sulphides, silica-rich glass) might have evaporated.

Conclusion

Various micro-structures, textures and inclusions in zircon and baddeleyite–zircon aggregates from impactites of the Apollo 15 and 16 landing sites were studied and discussed. Many features are interpreted to be related to one or multiple shock events and can be related to different stages of shock and subsequent heating processes. Recognition of such features and their accurate interpretation is an important basis for the interpretation of isotopic ages obtained on the same minerals. The features include:

1. Planar and non-planar fractures, with or without associated offsets. These are likely a result of high shear stresses during the unloading of the shock wave.
2. Thick columnar or granular zircon rims around baddeleyite. These form as a result of shock-induced local melting of Si-rich surrounding phases.
3. Granular textured zircon that results from shock-related melting and recrystallization of zircon at temperatures above the melting point of ZrO$_2$ (ca. 2715 °C and above).
4. Zircon granules containing monoclinic, tetragonal and cubic ZrO$_2$, and rutile inclusions and amorphous SiO$_2$-rich glass at triple junctions. The zircon granules are composed of nanocrystalline units forming mosaic crystals—a result of rapid crystallization.
5. Amorphous material formed by shock-induced decomposition of zircon or formation of diaplectic glass as a result of high shock pressure.
6. Recrystallized domains in zircons are evidence of annealing that in lunar crust could have been caused by heating from subsequent impact events.

Despite the presence of a great variety of zircon microstructures, studied zircon grains display a relatively uniform distribution of ^{207}Pb/^{206}Pb ages near 4200–4210 Ma (one granular aggregate, being ca. 50 Ma younger). Such remarkable consistency in ages either reflects (i) a small time difference between impact-related recrystallization that led to and secondary impact-induced deformation and amorphization, or (ii) resistance of amorphous or nanocrystalline domains in lunar impactite zircon to later shock-induced Pb loss.

References

Anderson AJ, Wirth R, Thomas R (2008) The alteration of metamict zircon and its role in the remobilization of high-field-strength elements in the Georgeville granite, Nova Scotia. Can Mineral 46:1–18

Bellucci JJ, Whitehouse MJ, Nemchin AA, Snape JF, Pidgeon RT, Grange M, Reddy SM, Timms N (2016) A scanning ion imaging investigation into the micron-scale U-Pb systematics in a complex lunar zircon. Chem Geol 438:112–122. https://doi.org/10.1016/j.chemgeo.2016.05.022

Bellucci JJ, Nemchin AA, Grange M, Robinson KL, Collins G, Whitehouse MJ, Snape JF, Norman MD, Kring DA (2019) Terrestrial-like zircon in a clast from an Apollo 14 breccia. Earth Planet Sc Lett 510:173–185. https://doi.org/10.1016/j.epsl.2019.01.010

Cavosie AJ, Erickson TM, Timms NE, Reddy SM, Talavera C, Montalvo SD, Pincus MR, Gibbon RJ, Moser D (2015) A terrestrial perspective on using ex situ shocked zircons to date lunar impacts. Geology 43:999–1002

Cavosie AJ, Timms NE, Erickson TM, Hagerty JJ, Hörz F (2016) Transformations to granular zircon revealed: twinning, reidite, and ZrO2 in shocked zircon from Meteor Crater (Arizona, USA). Geology 44(9):703–706. https://doi.org/10.1130/G38043.1

Cavosie AJ, Erickson TM, Montalvo PE, Prado DC, Cintron NO, Gibbon RJ (2018a) The Rietputs formation in South Africa: a Pleistocene fluvial archive of meteorite impact unique to the Kaapvaal craton. In: Moser DE, Corfu F, Reddy SM, Darling J, Tait K (eds) Microstructural geochronology: lattice to atom-scale records of planetary evolution, vol. AGU-Wiley, New Jersey, pp 203–224

Cavosie AJ, Timms NE, Ferrière L, Rochette P (2018b) FRIGN zircon—the only terrestrial mineral diagnostic of high-pressure and high-temperature shock deformation. Geology 46(10):891–894. https://doi.org/10.1130/G45079.1

Chevalier J, Gremillard L, Virkar AV, Clarke DR (2009) Tetragonal-monoclinic transformation in zirconia: lessons learned and future trends. J Am Ceram Soc 92:1901–1920

Corfu F, Hanchar JM, Hoskin PWO, Kinny P (2003) Atlas of zircon textures. Rev Mineral Geochem 53(1):469–500. https://doi.org/10.2113/0530469

Crow CA, McKeegan KD, Moser DE (2017) Coordinated U-Pb geochronology, trace element, Ti-in-zircon thermometry and microstructural analysis of Apollo zircons. Geochim Cosmochim Acta 202:264–284. https://doi.org/10.1016/j.gca.2016.12.019

Crow CA, Moser DE, McKeegan KD (2019) Shock metamorphic history of >4 Ga Apollo 14 and 15 zircons. Meteorit Planet Sci 54(1):181–201. https://doi.org/10.1111/maps.13184

Darling JR, Moser DE, Barker IR, Tait KT, Chamberlain KR, Schmitt AK, Hyde BC (2016) Variable microstructural response of baddeleyite to shock metamorphism in young basaltic shergottite NWA 5298 and improved U-Pb dating of Solar System events. Earth Planet Sci Lett 444:1–12

Davidson A, van Breemen O (1988) Baddeleyite-zircon relationships in coronitic metagabbro, Grenville Province, Ontario: implications for geochronology. Contrib Mineral Petrol 100:291–299

Davis DW, Williams IS, Krogh TE (2003) Historical development of zircon geochronology. Rev Mineral Geochem 53:145–181

Deer WA, Howie RA, Zussman J (1997) Rock-forming minerals. Orthosilicates. Mineralogical Society of Great Britain and Ireland, ISBN: 0903056275

Dunkley DJ, Kusiak MA, Wilde SA, Whitehouse MJ, Sałacińska A, Kielman R, Konečný P (2020) Two Neoarchean tectonothermal events on the western edge of the North Atlantic Craton, as revealed by SIMS dating of the Saglek Block, Nain Province, Labrador. J Geol Soc London 177:31–49. https://doi.org/10.1144/jgs2018-153

Dürr TA, Becker H, Schwarz WH, Vanderliek D (2021) Testing the origin of impactites at the Apollo 17 landing site: U-PB ages of baddeleyite in breccia 77035. 52nd Lunar and Planetary Science Conference 2021 (LPI Contrib. No. 2548): 1951

Fernandes VA, Fritz J, Weiss BP, Garrick-Bethell I, Shuster DL (2013) The bombardment history of the Moon as recorded by 40Ar-39Ar chronology. Meteorit Planet Sci 48(2):241–269. https://doi.org/10.1111/maps.12054

Gleiter H (1989) Nanocrystalline materials. Prog Mater Sci 33:233–315

Grange ML, Nemchin AA, Pidgeon RT, Timms N, Muhling JR, Kennedy AK (2009) Thermal history recorded by the Apollo 17 impact melt breccia 73217. Geochim Cosmochim Acta 73:3093–3107

Grange ML, Nemchin AA, Pidgeon RT (2013a) The effect of 1.9 and 1.4 Ga impact events on 4.3 Ga zircon and phosphate from an Apollo 15 melt breccia. J Geophys Res-Planet 118(10):2180–2197. https://doi.org/10.1002/Jgre.20167

Grange ML, Pidgeon RT, Nemchin AA, Timms NE, Meyer C (2013b) Interpreting U-Pb data from primary and secondary features in lunar zircon. Geochim Cosmochim Acta 101:112–132. https://doi.org/10.1016/j.gca.2012.10.013

Gucsik A, Koerberl C, Brandstätter F, Reimold WU, Libowitzky E (2002) Cathodoluminescence, electron microscopy, and Raman spectroscopy of experimentally shock-metamorphosed zircon. Earth Planet Sci Lett 202:495–509

Gucsik A, Koerberl C, Brandstätter F, Libowitzky E, Reimold WU (2004) Cathodoluminescence, electron microscopy, and Raman spectroscopy of experimentally shock metamorphosed zircon crystals and naturally shocked zircon from the Ries impact crater. In: Dypvik H, Burchell M, Claeys Ph (eds) Cratering in marine environments and on ice. Springer-Verlag, Heidelberg, Germany, pp 281–322

Heaman LM, Lecheminant AN (1993) Paragenesis and U-Pb systematics of baddeleyite (Zro2). Chem Geol 110(1–3):95–126. https://doi.org/10.1016/0009-2541(93)90249-I

Kaiser A, Lobert M, Telle R (2008) Thermal stability of zircon (ZrSiO4). J Eur Ceram Soc 28(11):2199–2211. https://doi.org/10.1016/j.jeurceramsoc.2007.12.040

Keller LP, Berger EL, Zhang S, Christoffersen R (2021) Solar energetic particle tracks in lunar samples: a transmission electron microscope calibration and implications for lunar space weathering. Meteorit Planet Sci 56:1685–1707

Kenny GG, Schmieder M, Whitehouse MJ, Nemchin AA, Morales LFG, Buchner E, Bellucci JJ, Snape JF (2019) A new U-Pb age for shock-recrystallised zircon from the Lappajärvi impact crater, Finland, and implications for the accurate dating of impact events. Geochim Cosmochim Acta 245:479–494. https://doi.org/10.1016/j.gca.2018.11.021

Kovaleva E, Habler G (2019) Spatial distribution of zircon with shock microtwins in pseudotachylite-bearing granite gneisses, Vredefort impact structure, South Africa. J Struct Geol 129:103890

Kovaleva E, Kusiak MA, Kenny G, Whitehouse MJ, Habler G, Schreiber A, Wirth R (2021) Nano-scale investigation of granular neoblastic zircon, Vredefort impact structure, South Africa: evidence for complete shock melting. Earth Planet Sci Lett 565:116948. https://doi.org/10.1016/j.epsl.2021.116948

Kusiak MA, Whitehouse MJ, Wilde SA, Nemchin AA, Clark C (2013) Mobilization of radiogenic Pb in zircon revealed by ion imaging: Implications for early Earth geochronology. Geology 41(3):291–294. https://doi.org/10.1130/g33920.1

Kusiak MA, Williams IS, Dunkley DJ, Konečný P, Słaby E, Martin H (2014) Monazite to the rescue: U-Th–Pb dating of the intrusive history of the composite Karkonosze pluton, Bohemian Massif. Chem Geol 364:76–92. https://doi.org/10.1016/j.chemgeo.2013.11.016

Kusiak MA, Dunkley DJ, Wirth R, Whitehouse MJ, Wilde SA, Marquardt K (2015) Metallic lead nanospheres discovered in ancient zircons. Proc Natl Acad Sci USA 112(16):4958–4963

Leroux H, Reimold WU, Koeberl C, Hornemann U, Doukhan JC (1999) Experimental shock deformation in zircon: a transmission electron microscopic study. Earth Planet Sci Lett 169(3):291–301. https://doi.org/10.1016/S0012-821X(99)00082-5

Lyon IC, Kusiak MA, Wirth R, Whitehouse MJ, Dunkley DJ, Wilde SA, Schaumlöffel D, Malherbe J, Moore KL (2019) Pb nanospheres in ancient zircon yield model ages for zircon formation and Pb mobilization. Sci Rep-Uk 9(1):13702. https://doi.org/10.1038/s41598-019-49882-8

Meyer C (2005) Lunar sample compedium. Technical report. NASA/STI Accession number: 20060011039

Moser DE, Davis WJ, Reddy SM, Flemming RL, Hart RJ (2009) Zircon U-Pb strain chronometry reveals deep impact-triggered flow. Earth Planet Sci Lett 277(1–2):73–79. https://doi.org/10.1016/J.Epsl.2008.09.036

Moser DE, Cupelli CL, Barker IR, Flowers RM, Bowman JR, Wooden J, Hart JR (2011) New zircon shock phenomena and their use for dating and reconstruction of large impact structures revealed by electron nanobeam (EBSD, CL, EDS) and isotopic U–Pb and (U–Th)/He analysis of the Vredefort domeThis article is one of a series of papers published in this special issue on the theme of geochronology in honour of Tom Krogh. Can J Earth Sci 48(2):117–139. https://doi.org/10.1139/E11-011

Moser DE, Chamberlain KR, Tait KT, Schmitt AK, Darling JR, Barker IR, Hyde BC (2013) Solving the Martian meteorite age conundrum using micro-baddeleyite and launch-generated zircon. Nature 499(7459):454–457. https://doi.org/10.1038/Nature12341

Nasdala L (2009) Pb+ irradiation of synthetic zircon (ZrSiO4): Infrared spectroscopic investigation-discussion. Am Mineral 94(5–6):853–855. https://doi.org/10.2138/Am.2009.541

Nasdala L, Irmer G, Wolf D (1995) The degree of metamictization in zircon—a Raman-spectroscopic study. Eur J Mineral 7(3):471–478

Nemchin A, Timms N, Pidgeon R, Geisler T, Reddy S, Meyer C (2009) Timing of crystallization of the lunar magma ocean constrained by the oldest zircon. Nat Geosci 2(2):133–136. https://doi.org/10.1038/Ngeo417

Nemchin AA, Grange ML, Pidgeon RT, Meyer C (2012) Lunar zirconology. Aust J Earth Sci 59(2):277–290. https://doi.org/10.1080/08120099.2011.613484

Nemchin AA, Tao L, Jolliff BL, Wan Y, Snape JF, Zeigler R, Grange ML, Liu D, Whitehouse MJ, Timms NE, Fred J (2021) Ages of lunar impact breccias: limits for timing of the Imbrium impact. Geochemistry 81(1):125683

Norman MD (2009) The Lunar Cataclysm: Reality or "Mythconception"? Elements 5(1):23–28. https://doi.org/10.2113/gselements.5.1.23

Norman MD, Nemchin A (2014) A 4.2 billion year old impact basin on the Moon: U-Pb dating of zirconolite and apatite in lunar melt rock 67955. Earth Planet Sc Lett 388:387–398

Norman MD, Taylor LA, Shih CY, Nyquist LE (2016) Crystal accumulation in a 4.2 Ga lunar impact melt. Geochim Cosmochim Acta 172:410–429

Piazolo S, Austrheim H, Whitehouse M (2012) Brittle-ductile microfabrics in naturally deformed zircon: deformation mechanisms and consequences for U-Pb dating. Am Miner 97:1544–1563

Piazolo S, La Fontaine A, Trimby P, Harley S, Yang L, Armstrong R, Cariney JM (2016) Deformation-induced trace element redistribution in zircon revealed using atom probe tomography. Nat Commun 7:20490. https://doi.org/10.1038/ncomms10490

Pidgeon RT, Nemchin AA, van Bronswijk W, Geisler T, Meyer C, Compston W, Williams IS (2007) Complex history of a zircon aggregate from lunar breccia 73235. Geochim Cosmochim Acta 71(5):1370–1381. https://doi.org/10.1016/J.Gca.2006.11.021

Pidgeon RT, Merle RE, Grange ML, Nemchin AA (2018) Annealing history of zircons from Apollo 14083 and 14303 impact breccias. Meteoriti Planet Sci. https://doi.org/10.1111/maps.13185

Rubatto D (2017) Zircon: the metamorphic mineral. Rev Mineral Geochem 83(1):261–295. https://doi.org/10.2138/rmg.2017.83.9

Snape JF, Nemchin AA, Grange ML, Bellucci JJ, Thiessen F, Whitehouse MJ (2016) Phosphate ages in Apollo 14 breccias: resolving multiple impact events with high precision U-Pb SIMS analyses. Geochim Cosmochim Acta 174:13–29. https://doi.org/10.1016/j.gca.2015.11.005

Takagi S, Ichiyanagi K, Kyono A, Kawai N, Nozawa S, Ozaki N, Seto Y, Okuchi T, Nitta S, Okada S, Miyanishi K, Sueda K, Togashi T, Yabuuchi T (2022) Phase transition and melting in zircon by nanosecond shock loading. Phys Chem Miner 49(5):8. https://doi.org/10.1007/s00269-022-01184-8

Telle R, Greffrath F, Prieler R (2015) Direct observation of the liquid miscibility gap in the zirconia–silica system. J Eur Ceram Soc 35:3995–4004

Thiessen F, Nemchin AA, Snape JF, Bellucci JJ, Whitehouse MJ (2018) Apollo 12 breccia 12013: impact-induced partial Pb loss in zircon and its implications for lunar geochronology. Geochim Cosmochim Acta 230:94–111. https://doi.org/10.1016/j.gca.2018.03.023

Timms NE, Reddy SM, Healy D, Nemchin AA, Grange ML, Pidgeon RT, Hart R (2012) Resolution of impact-related microstructures in lunar zircon: a shock-deformation mechanism map. Meteorit Planet Sci 47(1):120–141. https://doi.org/10.1111/J.1945-5100.2011.01316.X

Timms NE, Erickson TM, Pearce MA, Cavosie AJ, Schmieder M, Tohver E, Reddy SM, Zanetti MR, Nemchin AA, Wittmann A (2017) A pressure-temperature phase diagram for zircon at extreme conditions. Earth-Sci Rev 165:185–202. https://doi.org/10.1016/j.earscirev.2016.12.008

Trail D, Barboni M, McKeegan KD (2020) Evidence for diverse lunar melt compositions and mixing of the pre-3.9 Ga crust from zircon chemistry. Geochim Cosmochim Acta 284:173–195

Vanderliek DM, Becker H, Rocholl A (2021a) Impact-related crystallization and modification of small zircons in Apollo 15 and 16 impactites at 4.2 Ga. Earth Planet Sc Lett 576:11726. https://doi.org/10.1016/j.epsl.2021.117216

Vanderliek DM, Becker H, Rocholl A, Schwarz WH (2021b) The behaviour of the U-Pb system in apatite and Zr minerals in pristine lunar norite during infiltration by imbrium impact melt. Goldschmidt Conf 2021. https://doi.org/10.7185/gold2021.6167

Wentworth SJ, Mckay DS (1991) Apollo-14 glasses and the origin of lunar soils. Proc Lunar Planet Sci 21:185–192

White LT, Ireland TR (2012) High-uranium matrix effect in zircon and its implications for SHRIMP U-Pb age determinations. Chem Geol 306:78–91. https://doi.org/10.1016/J.Chemgeo.2012.02.025

White LF, Darling JR, Moser DE, Cayron C, Barker I, Dunlop J, Tait KT (2018) Baddeleyite as a widespread and sensitive indicator of meteorite bombardment in planetary crusts. Geology 46(8):719–722. https://doi.org/10.1130/g45008.1

White LF, Moser DE, Tait KT, Langelier B, Barker I, Darling JR (2019) Crystallization and impact history of a meteoritic sample of early lunar crust (NWA 3163) refined by atom probe geochronology. Geosci Front 10(5):1841–1848. https://doi.org/10.1016/j.gsf.2018.11.005

White LF, Černok A, Darling JR, Whitehouse MJ, Joy KH, Cayron C, Dunlop J, Tait KT, Anand M (2020) Evidence of extensive lunar crust formation in impact melt sheets 4,330 Myr ago. Nature Astronomy 4:974–978

Wielicki MM, Harrison TM (2015) Zircon formation in impact melts: complications for deciphering planetary impact histories. In: Osinski GR, Kring DA (eds) Large meteorite impacts and planetary evolution V. Geological Society of America Special Paper 518, Boulder, pp 127–134. https://doi.org/10.1130/2015.2518(08)

Williams IS, Hergt JM (2000) U-Pb dating of Tasmanian dolerites: a cautionary tale of SHRIMP analysis of high-U zircon. In: Woodhead JD, Hergt JM, Noble WP (eds) Beyond 2000: new frontiers in isotope geoscience. Abstr Proc, Lorne, pp 185–188

Wingate MTD, Campbell IH, Compston W, Gibson GM (1998) Ion microprobe U-Pb ages for Neoproterozoic basaltic magmatism in south-central Australia and implications for the breakup of Rodinia. Precambr Res 87:135–159

Wirth R (2009) Focused Ion Beam (FIB) combined with SEM and TEM: advanced analytical tools for studies of chemical composition, microstructure and crystal structure in geomaterials on a nanometre scale. Chem Geol 261:217–229

Wittmann A, Kenkmann T, Schmitt RT, Stöffler D (2006) Shock-metamorphosed zircon in terrestrial impact craters. Meteorit Planet Sci 41:433–454

Wittmann A, Cavosie AJ, Timms NE, Ferrière L, Rae A, Rasmussen C, Ross C, Stockli D, Schmieder M, Kring DA, Zhao J, Xiao L, Morgan JV, Gulick SPS, the IODP-ICDP Expedition 364 Scientists (2021) Shock impedance amplified impact deformation of zircon in granitic rocks from the Chicxulub impact crater. Earth Planet Sci Lett 575:117201

Zhang AC, Hsu WB, Li XH, Ming HL, Li QL, Liu Y, Tang GQ (2011) Impact melting of lunar meteorite Dhofar 458: evidence from polycrystalline texture and decomposition of zircon. Meteorit Planet Sci 46(1):103–115. https://doi.org/10.1111/J.1945-5100.2010.01144.X

Zhou Q, Herd CDK, Yin QZ, Li XH, Wu FY, Li QL, Liu Y, Tang GQ, McCoy TJ (2013) Geochronology of the Martian meteorite Zagami revealed by U-Pb ion probe dating of accessory minerals. Earth Planet Sc Lett 374:156–163. https://doi.org/10.1016/J.Epsl.2013.05.035